

Constraints on the Symmetry Energy Using the Mass-Radius Relation of Neutron Stars

James M. Lattimer¹ and Andrew W. Steiner²

¹ Dept. of Physics & Astronomy, Stony Brook University, Stony Brook, NY 11794-3800, USA

² Institute for Nuclear Theory, Seattle, WA 98195, USA

Received: date / Revised version: date

Abstract. The nuclear symmetry energy is intimately connected with nuclear astrophysics. This contribution focuses on the estimation of the symmetry energy from experiment and how it is related to the structure of neutron stars. The most important connection is between the radii of neutron stars and the pressure of neutron star matter in the vicinity of the nuclear saturation density n_s . This pressure is essentially controlled by the nuclear symmetry energy parameters S_v and L , the first two coefficients of a Taylor expansion of the symmetry energy around n_s . We discuss constraints on these parameters that can be found from nuclear experiments. We demonstrate that these constraints are largely model-independent by deriving them qualitatively from a simple nuclear model. We also summarize how recent theoretical studies of pure neutron matter can reinforce these constraints. To date, several different astrophysical measurements of neutron star radii have been attempted. Attention is focused on photospheric radius expansion bursts and on thermal emissions from quiescent low-mass X-ray binaries. While none of these observations can, at the present time, determine individual neutron star radii to better than 20% accuracy, the body of observations can be used with Bayesian techniques to effectively constrain them to higher precision. These techniques invert the structure equations and obtain estimates of the pressure-density relation of neutron star matter, not only near n_s , but up to the highest densities found in neutron star interiors. The estimates we derive for neutron star radii are in concordance with predictions from nuclear experiment and theory.

PACS. 21.65.Cd nuclear matter – 26.60.-c nuclear matter aspects of neutron stars – 26.60.Kp equations of state – 97.60.Jd Neutron stars

1 Introduction

Neutron stars are laboratories for the study of dense nuclear matter under conditions that are beyond those that can be achieved in experiments. The equation of state and internal compositions of large portions of neutron stars are poorly understood at present. However, there has been substantial recent progress in unraveling these mysteries. This progress has come from theoretical studies of nuclear and neutron matter, nuclear experiments, and astrophysical observations. The most profound aspect of the nuclear interaction for neutron stars, in many respects, concerns the nuclear symmetry energy which largely controls the composition and pressure of neutron-rich matter, and therefore, many aspects of neutron star structure such as the radius, moment of inertia and crustal properties.

For most practical purposes, the interior of a neutron star can be divided into a dense core and a less-dense crust. The density of the core-crust boundary is believed to be near $n_s/2$, where $n_s \simeq 0.16 \text{ fm}^{-3}$ is the nuclear saturation density, with a weak dependence on the incompressibility and symmetry properties of bulk nuclear matter. While matter just below the neutron star crust is likely a uniform liquid of hadrons, electrons and muons, the crust it-

self is composed of an equilibrium mixture of dense nuclei and a neutron gas together with electrons. This division into two coexisting phases is a natural consequence of the fact that uniform nuclear matter at subnuclear densities, for large proton fractions, has negative pressure. For these densities, phase coexistence involves pressure and neutron and proton chemical potential equality in both phases, which together determine the relative concentrations of nuclei (the dense phase) and neutron gas (the less dense phase). It is important to point out that in the crust the pressure mostly originates from the degenerate relativistic electrons, for which the pressure is $p_e = \hbar c n x (3\pi^2 n x)^{1/3}$, where n is the baryon density and x is the proton fraction (charge neutrality dictates that the number of electrons per baryon is also x). Baryon pressure originates from both nuclei and the neutron gas. However, the overall pressure of a nucleus must equal the neutron gas pressure, or it would expand or contract. This pressure remains very small until densities approach n_s . In fact, the dominant baryonic pressure results from the attractive Coulomb energy stemming from the Coulomb lattice, leading to a net negative pressure that, like p_e , scales as $n^{4/3}$. The ratio of the magnitudes of the lattice and electron pressures

is only a few percent, however, so in spite of uncertainties regarding the nuclear force, the equation of state (at least, the pressure-density relation) in the crust is very well-understood.

Matter in the interior of a neutron star, unlike that in laboratory nuclei, is very neutron rich. On timescales long compared to β decay timescales of seconds, neutron star matter evolves into weak interaction equilibrium, or β -equilibrium, in which the total energy is at a minimum with respect to composition:

$$\frac{\partial(E + E_e)}{\partial x} = \mu_p - \mu_n + \mu_e - (m_n - m_p)c^2 = 0, \quad (1)$$

where E is the baryon energy per baryon and E_e is the electron energy per baryon. The μ s are chemical potentials, which, for baryons, are measured with respect to their rest masses. Electrons are relativistic, and $\mu_e = \hbar c(3\pi^2 n_x)^{1/3}$. The energy of uniform hadronic matter, in its ground state, is essentially a function of baryon density (n), temperature (T), and composition, which is usually parameterized in terms of its charge fraction x . For baryonic matter composed solely of neutrons and protons, $x = n_p/(n_n + n_p)$. It is convenient to define the symmetry energy $S(n)$ as the difference between the energy per baryon of pure neutron matter ($x = 0$) and symmetric nuclear matter ($x = 1/2$). Since matter in neutron stars under nearly all conditions of interest here is highly degenerate, we only consider the case $T = 0$.

In most theoretical models of cold uniform nuclear matter, the energy at a given density can be well approximated by keeping only the first term of a quadratic expansion:

$$E(n, x) \simeq E(n, 1/2) + S_2(n)(1 - 2x)^2 + \dots \quad (2)$$

so that the symmetry energy $S(n) \simeq S_2(n)$. However, it has not been experimentally verified that quartic and higher-order terms are negligible. We will indicate where this neglect might have an appreciable effect. The symmetry energy is experimentally accessible from nuclear masses and other experiments such as dipole resonances and neutron skin thicknesses which sample matter near the nuclear saturation density n_s . It is therefore convenient to consider a Taylor expansion of S_2 near n_s :

$$S_2(n) \simeq S_v + \frac{L}{3}(n - n_s) + \frac{K_{\text{sym}}}{18}(n - n_s)^2 + \dots \quad (3)$$

which defines the symmetry parameters S_v , L and K_{sym} .

From Equation (2), we now find that

$$\mu_p - \mu_n = \frac{\partial E}{\partial x} = 4S_2(n)(1 - 2x). \quad (4)$$

The solution of Equation (1) at n_s yields

$$x \simeq \frac{1}{3\pi^2 n_s} \left(\frac{4S_v}{\hbar c} \right)^3 \simeq 0.04, \quad (5)$$

i.e., neutron star matter is very nearly pure neutron matter. At higher densities, x follows the behavior of $S_2(n)$.

Below n_s , where nuclei exist, Equation (4) shows that the neutron excess of the system, and individual nuclei, increases with density. The minimum value of x in beta equilibrium generally occurs at the core-crust boundary just below n_s .

For pure neutron matter at n_s and in the quadratic approximation, the energy and pressure are given by

$$\begin{aligned} E_N(n_s) &= E(n, 0) \simeq S_v + B, \\ p_N(n_s) &= p(n_s, 0) = n_s^2 \left(\frac{\partial E}{\partial n} \right)_{n_s, x=0} \simeq \frac{L}{3} n_s, \end{aligned} \quad (6)$$

where $B = -E(n_s, 1/2) \simeq 16$ MeV is the binding energy of symmetric matter at the saturation density. For matter in β -equilibrium, it follows that

$$p_\beta(n_s) \simeq \frac{L}{3} n_s \left[1 - \left(\frac{4S_v}{\hbar c} \right)^3 \frac{4 - 3S_v/L}{3\pi^2 n_s} + \dots \right]. \quad (7)$$

This important result shows that the pressure of matter at the nuclear saturation density can be expressed solely in terms of the standard symmetry parameters S_v and L , in the quadratic approximation.

The symmetry energy is not only important in determining the composition and pressure of matter in the interior, but also plays an important role in determining the overall structure of the star. Lattimer & Prakash [1] found that the neutron star radius R , for a given stellar mass M , is highly correlated with the neutron star matter pressure p_β at densities in the vicinity of n_s . This relation can be expressed as

$$R_M = C(n, M)[p_\beta(n)/\text{MeV fm}^{-3}]^{1/4}, \quad (8)$$

where R_M is the radius of a star of mass M and C are coefficients that depend on the density and mass. The upper set in table 1 shows the coefficients $C(n, 1.4M_\odot)$ compiled from about 3 dozen equations of state for three densities, n_s , $1.5n_s$ and $2n_s$. Lattimer & Lim [2] re-analyzed this relation restricted to EOSs which could satisfy the constraint $\hat{M} = 2.0M_\odot$ where \hat{M} is the minimum value for the maximum neutron star mass given by the largest precisely measured neutron star mass. Currently, this determined from measurements of PSR J1614+2230 [3], with $M = 1.97 \pm 0.04M_\odot$, and PSR J0348+0432 [4], with $M = 2.01 \pm 0.04M_\odot$. It is observed that the coefficients $C(n, M)$ become more accurate at higher densities, but since p_β can be expressed relatively model-independently in terms of S_v and L at $n = n_s$, we can only usefully employ $C(n_s, 1.4M_\odot)$ to relate neutron star radii to symmetry energy parameters.

2 Symmetry Parameters From Nuclear Experiments

2.1 Correlations from the liquid drop model

The distribution of neutrons and protons within nuclei differ, and, furthermore, these distributions vary with Z

Table 1. Coefficients $C(n, 1.4M_\odot)$, in km, for the pressure-radius correlation. \hat{M} is the minimum value for the maximum neutron star mass.

\hat{M}/M_\odot	n_s	$1.5n_s$	$2n_s$
1.3	9.30 ± 0.58	6.99 ± 0.30	5.72 ± 0.25
2.0	9.52 ± 0.49	7.06 ± 0.24	5.68 ± 0.14

and A . Therefore, measurements of nuclear properties, especially for neutron-rich nuclei, offer hope of constraining nuclear symmetry energy parameters. The most obvious manifestation of the effects of symmetry is visible in the liquid drop expression of the nuclear energy

$$E(Z, A) = A(-B + S_v I^2) + A^{2/3}(E_s - S_s I^2) + \frac{3}{5} \frac{e^2 Z^2}{r_0 A^{1/3}} + E_{\text{shell}}(Z, A - Z) + E_{\text{pairing}}(A), \quad (9)$$

where $E_s \simeq 19$ MeV is the symmetric matter surface energy parameter, $I = (A - 2Z)/A$ is the neutron excess, S_s is the surface symmetry energy parameter, and $r_0 = (4\pi n_s/3)^{-1/3}$. The last three terms in Eq. (9) represent the Coulomb, shell and pairing energies, respectively. We will ignore shell and pairing effects for the present discussion.

The net symmetry energy of an isolated nucleus is then

$$E_{\text{DM},i} = I_i^2(S_v A_i - S_s A_i^{2/3}). \quad (10)$$

The parameters of the liquid drop model are typically determined by a least-squares fit to measured masses, so a linear correlation between S_v and S_s is therefore expected from minimizing the differences between model predictions and experimentally measured symmetry energies, i.e., minimizing

$$\chi^2 = \sum_i (E_{\text{exp},i} - E_{\text{DM},i})^2 / \sigma_{\text{DM}}^2, \quad \bar{\chi}^2 \equiv \chi^2 / \mathcal{N} \quad (11)$$

where \mathcal{N} is the total number of nuclei and σ_{DM} is a nominal error. A $\bar{\chi}^2$ contour one unit above the minimum value represents the $1 - \sigma$ confidence interval which is an ellipse in this linear example.

The properties of the confidence ellipse are determined by the second derivatives of $\bar{\chi}^2$ at the minimum,

$$[\bar{\chi}_{vv}, \bar{\chi}_{vs}, \bar{\chi}_{ss}] = \frac{2}{\mathcal{N} \sigma_{\text{DM}}^2} \sum_i I_i^4 [A_i^2, -A_i^{5/3}, A_i^{4/3}] \simeq [61.6, -10.7, 1.87] / \sigma_{\text{DM}}^2, \quad (12)$$

where $\bar{\chi}_{vs} = \partial^2 \bar{\chi}^2 / \partial S_v \partial S_s$, etc. The specific values quoted follow from the set of 2336 nuclei with N and Z greater than 40 from Ref. [5]. The confidence ellipse in $S_s - S_v$ space has orientation $\alpha_{\text{DM}} = (1/2) \tan^{-1} |2\bar{\chi}_{vs} / (\bar{\chi}_{vv} - \bar{\chi}_{ss})| \simeq 9.8^\circ$ with respect to the S_s axis, with error widths $\sigma_{v,\text{DM}} = \sqrt{(\bar{\chi}^{-1})_{vv}} \simeq 2.3\sigma_{\text{DM}}$ and $\sigma_{s,\text{DM}} = \sqrt{(\bar{\chi}^{-1})_{ss}} \simeq 13.2\sigma_{\text{DM}}$ where $(\bar{\chi}^{-1})$ is the matrix inverse. The correlation coefficient is $r_{\text{DM}} = \bar{\chi}_{vs} / \sqrt{\bar{\chi}_{vv}\bar{\chi}_{ss}} \simeq 0.997$. In this

simple example, the shape and orientation of the confidence interval depend only on A_i and I_i and not on the binding energies themselves or the location of the $\bar{\chi}^2$ minimum or the other drop parameters. This correlation is therefore largely model-independent and the most valuable of constraints from nuclear experiment.

In practice, the liquid droplet model [6], which differs from the liquid drop model by accounting for varying neutron/proton ratios within the nucleus that produce neutron skins in neutron-rich nuclei, is an improved treatment. Its symmetry energy is

$$E_{\text{LD},i} = S_v I_i^2 A_i (1 + S_s A_i^{-1/3} / S_v)^{-1}, \quad (13)$$

and therefore predicts a linear correlation between S_s/S_v and S_v rather than between S_s and S_v as in the drop model. The same methodology as for the liquid drop model can be used to determine the confidence interval in $S_s/S_v - S_v$ space. In contrast to the drop model, the properties of the confidence interval now also depend, but only slightly, on the measured masses, $E_{\text{exp},i}$, as well as the parameters of the droplet model.

The liquid droplet model also predicts correlations from other observational properties of nuclei. These include the dipole polarizability, which is the linear response of a nucleus excited from its ground state to an excited state due to the action of an external isovector oscillating (dipole) electric field,

$$\alpha_D = \frac{AR^2}{20S_v} \left[1 + \frac{5}{3} \frac{S_s}{S_v} A^{-1/3} \right], \quad (14)$$

where $R = r_0 A^{1/3}$ is the nuclear radius, and the neutron skin thickness

$$R_n - R_p = \frac{2r_0}{3} \frac{S_s I}{S_v + S_s A^{-1/3}}, \quad (15)$$

where $R_{n,p}$ are the mean neutron and proton radii.

Comparing the functional forms of Equations (13), (14) and (15), we observe that, respectively keeping E_{LD} , α_D and $R_n - R_p$ fixed, different slopes are predicted for variations of S_s/S_v relative to S_v :

$$\frac{d(S_s/S_v)}{dS_v} = \frac{1}{S_v} \left[A^{1/3} + \frac{S_s}{S_v}, \frac{3}{5} A^{1/3} + \frac{S_s}{S_v}, 0 \right] \simeq [0.25, 0.17, 0] \text{ MeV}^{-1}, \quad (16)$$

where we assumed $S_v \simeq 30$ MeV, $S_s/S_v \simeq 3/2$ and $A^{1/3} \simeq 6$. As a result, comparison of experimental results for these nuclear properties can potentially tightly constrain the liquid droplet symmetry parameters, S_v and S_s .

However, we have seen that astrophysical constraints on the neutron star radius restrict the value of $p_\beta(n_s)$, which can be expressed in terms of S_v and L via Equation (7). To make nuclear experimental constraints astrophysically relevant therefore requires them to be expressed in $S_v - L$ space rather than $S_v - S_s$ space. In the context of the liquid droplet model, the surface energy term represents the correction to the volume energy which accounts

for the fact that the density within the nucleus is not constant. Therefore, we can expect that the density dependence of S (or S_2) is critical to this transformation and we can write $S_s(S_2)$ in the quadratic approximation.

One can analytically predict these liquid droplet correlations as well as the relation $S_s(S_2)$ by means of the so-called *hydrodynamical* model proposed by Lipparini & Stringari [7]. If S_2 could be adequately described in the density range $0 < n < n_s$ with only the parameters S_v and L , this automatically would lead to an expression for $S_s(S_v, L)$. The original model [7] assumed $S_2(n) = S_v + L(n - n_s)/3$, which is strictly valid only as long as $n/|n - n_s| \ll 1$. As a result, the relation for $S_s(S_v, L)$ and the experimental correlations between S_v and L estimated in Ref. [7] are model-dependent. Here, we generalize the model to allow for an arbitrary dependence of S_2 on the density so that the model-dependence of higher-order terms in the density expansion of S_2 , such as K_{sym} , can be determined.

We emphasize that the hydrodynamical model is not a substitute for more sophisticated microscopic treatments of nuclei, including Thomas-Fermi and Hartree-Fock analyses. However, it does allow one to straightforwardly observe the origins of correlations between S_v and L that have been proposed to result from nuclear experiments.

2.2 The hydrodynamical model

Following Lipparini & Stringari, we assume a simplified nuclear Hamiltonian energy density

$$\begin{aligned} \mathcal{H} &= \mathcal{H}_B(n, \alpha) + \mathcal{Q}(n) (n')^2, \\ \mathcal{H}_B(n, \alpha) &= \mathcal{H}_B(n, 0) + v_{sym}(n) \alpha^2 \end{aligned} \quad (17)$$

where the uniform matter contribution is $\mathcal{H}_B(n, \alpha)$, $\mathcal{Q}(n)$ controls the gradient contributions, $v_{sym} = S_2/n$, $n = n_n + n_p$ is the isoscalar density, and $\alpha = n_n - n_p$ is the isovector density. We will optimize the total nuclear energy subject to the constraints

$$A = \int \rho d^3r, \quad N - Z = \int \alpha d^3r, \quad (18)$$

producing the chemical potentials μ and $\bar{\mu}$:

$$\frac{\delta}{\delta n} [\mathcal{H} - \mu n] = 0, \quad \frac{\delta}{\delta \alpha} [\mathcal{H} - \bar{\mu} \alpha] = 0. \quad (19)$$

These lead to

$$\begin{aligned} 2 \frac{d}{dr} [\mathcal{Q} n'] - \frac{\partial \mathcal{Q}}{\partial n} (n')^2 &= \frac{\partial \mathcal{H}_B}{\partial n} - \mu, \\ 0 &= \frac{\partial \mathcal{H}_B}{\partial \alpha} - \bar{\mu} = 2v_{sym} \alpha - \bar{\mu}. \end{aligned} \quad (20)$$

Using the second of the constraints (Equation 18) and the second of Equation (20), we obtain

$$N - Z = \frac{\bar{\mu}}{2} \int \frac{1}{v_{sym}} d^3r \equiv \frac{\bar{\mu}}{2} H, \quad (21)$$

which defines H . It then follows that

$$\alpha = \frac{\bar{\mu}}{2v_{sym}} = \frac{N - Z}{v_{sym} H}. \quad (22)$$

Separating out the total symmetry energy, and neglecting the Coulomb energy for the moment, we obtain

$$E_{sym0} = \int v_{sym} \alpha^2 d^3r = \frac{(N - Z)^2}{H}. \quad (23)$$

The dipole static polarizability, α_D , hereafter referred to simply as the dipole polarizability, is found by performing the constrained variation [7]

$$\frac{\delta}{\delta \alpha} \left(\int \mathcal{H} d^3r - \epsilon \int z \alpha d^3r \right) = 0, \quad (24)$$

with ϵ a small parameter. Defining α_d as the function $\alpha(r)$ which solves Eq. 24, the dipole polarizability is

$$\alpha_D = \frac{1}{2\epsilon} \int z \alpha_d d^3r. \quad (25)$$

The solutions for α_d and the dipole polarizability are

$$\alpha_d = \frac{\epsilon z}{2v_{sym}}, \quad \alpha_D = \frac{1}{12} \int \frac{r^2}{v_{sym}} d^3r, \quad (26)$$

where $z^2 = r^2/3$ within the integral. It is also possible to show [7] that the mean excitation energy ω_D of the dipole resonance is

$$\hbar^2 \omega_D^2 = \frac{\hbar^2}{3mA} \int v_{sym} n'^2 d^3r \quad (27)$$

The neutron skin thickness $R_n - R_p$, the difference between the mean radii of neutrons and protons, is defined by

$$\frac{4\pi}{3} (R_n^3 - R_p^3) = \int \left(\frac{n_n}{n_{no}} - \frac{n_p}{n_{po}} \right) d^3r \quad (28)$$

where n_{no} and n_{po} are the central values of the neutron and proton densities. R_n and R_p represent the 'squared-off' radii. From Equation (22), the central isovector density is

$$\alpha_o = \frac{N - Z}{v_{sym,o} H} = \frac{(N - Z)n_o}{S_v H}, \quad (29)$$

where n_o is the central density, which for symmetric matter would be n_s . $v_{sym,o} = S_v/n_o$ is the central value of v_{sym} . One can then show, treating $R_n - R_p \ll R$ and keeping the lowest-order term:

$$\frac{R_n - R_p}{R} \simeq \frac{2I}{3} \left(1 - \frac{A}{S_v H} \right) \left(1 - \frac{(N - Z)^2}{S_v^2 H^2} \right)^{-1}, \quad (30)$$

where $I = (N - Z)/A$.

Experimentally, however, it is preferable to measure the differences of the mean-square neutron and proton radii,

$$r_{np} = r_n - r_p \equiv \sqrt{\frac{\int n_n r^2 d^3r}{\int n_n d^3r}} - \sqrt{\frac{\int n_p r^2 d^3r}{\int n_p d^3r}}, \quad (31)$$

which, if the densities are uniform, is $\sqrt{3/5}(R_n - R_p)$. In the hydrodynamical model, the mean-square radii are

$$\begin{aligned} r_{n,p}^2 &= \frac{1}{(N, Z)} \int n_{n,p} r^2 d^3r = \frac{1}{2(N, Z)} \int (n \pm \alpha) r^2 d^3r \\ &= \frac{1}{1 \pm I} \left[\frac{3}{5} R^2 \pm 12 \frac{I \alpha_D}{H} \right], \end{aligned} \quad (32)$$

where the upper (lower) sign refers to $n(p)$. We then find

$$\frac{r_{np}}{R} \simeq I \sqrt{\frac{3}{5(1-I^2)} \left[\frac{20\alpha_D}{HR^2} - 1 \right]}. \quad (33)$$

This relation shows a clear connection between the neutron skin thickness and the dipole polarizability.

Now we focus on the behavior of the total density as a function of radius. Multiplying the first of Equation (20) by n' and the second by α' , their sum can be integrated:

$$\mathcal{Q}(n)n'^2 = \mathcal{H}_B(n, \alpha) - \mu n - \bar{\mu} \alpha, \quad (34)$$

for which the boundary condition $\mu n_o + \bar{\mu} \alpha_o = \mathcal{H}_B(n_o, \alpha_o)$ at the center. To make further progress, it is necessary to have specific functional forms for $\mathcal{H}_B(n, 0)$ and $\mathcal{Q}(n)$.

We make the common quadratic approximation for the uniform symmetric matter energy density:

$$\mathcal{H}_B(n, 0) = n \left[-B + \frac{K}{18} (1-u)^2 \right] \quad (35)$$

with compressibility parameter K , bulk binding energy B , and $u = \rho/\rho_s$, where ρ_s is the saturation density. In the case that $\alpha_o \simeq 0$, one has $\rho_o = \rho_s = 0.16 \text{ MeV fm}^{-3}$. When $\alpha_o > 0$, we can redefine n_s to be the new central density and B to the new bulk binding for that neutron excess, and still keep the quadratic behavior for $\mathcal{H}_B(n, 0)$. With the choice $\mathcal{Q}(n) = Q/n$, we now find the equation for the isoscalar density as a function of position:

$$\frac{du}{dz} = -u(1-u), \quad a = 3\sqrt{\frac{2Q}{K}}, \quad (36)$$

where $u = n/n_s$ and $z = r/a$, which defines the surface thickness parameter a . This has the solution of a Fermi function, or Woods-Saxon distribution,

$$u = \frac{1}{1 + e^{z-y}} \quad (37)$$

where y is a constant of integration, determined from the first constraint:

$$\begin{aligned} A &= \int n d^3r = 4\pi n_o a^3 F_2(y), \\ F_i(y) &= \int_0^\infty \frac{z^i dz}{1 + e^{z-y}} \simeq \frac{y^{i+1}}{i+1} \left[1 + \frac{i(i+1)}{6} \left(\frac{\pi}{y} \right)^2 \right]. \end{aligned} \quad (38)$$

Here F_i is the usual Fermi integral, and the right-most approximation holds for $y \gg 1$ and $i \neq -1$, ignoring an exponentially small term. This is justified, since one

finds that $y \simeq r_o A^{1/3}/a \simeq 13$ for ^{208}Pb (the value for a is determined below). The choice of $\mathcal{Q}(n)$ results in the Woods-Saxon density distribution assumed by Ref. [7].

The parameter $K \simeq 240 \text{ MeV}$ from experiment, and the value of Q follows from the observed value of the 90-10 surface thickness:

$$t_{90-10} = a \int_{0.1}^{0.9} \frac{du}{u'} = 4a \ln(3) \simeq 2.3 \text{ fm}, \quad (39)$$

giving $a = 0.523 \text{ fm}$ and

$$Q = \frac{K}{18} \left(\frac{t_{90-10}}{4 \ln(3)} \right)^2 \simeq 3.65 \text{ MeV fm}^2. \quad (40)$$

As a check, the liquid droplet surface tension parameter is the semi-infinite, symmetric matter, surface thermodynamic potential per unit area:

$$\begin{aligned} \sigma_o &= \int [\mathcal{H} - \mu n] dz = 2Q \int_0^\infty \frac{n'^2}{n} dz \\ &= \frac{2Q n_o}{a} \int_0^1 (1-u) du = \frac{Q n_o}{a} \simeq 1.17 \text{ MeV fm}^{-2}. \end{aligned} \quad (41)$$

This gives a value $E_s = 4\pi r_o^2 \sigma_o \simeq 19.2 \text{ MeV}$ for the symmetric matter surface energy parameter in the liquid droplet model, which is very close to the accepted value [6,8]. Therefore, the simple energy density functional we assume fits the most important observed properties of the symmetric matter nuclear interface, its tension and thickness, as well as the observed nuclear incompressibility.

Although Lipparini and Stringari assumed a simple form for $v_{sym}(n)$, this is not necessary to find analytic solutions. We note that the function $S_2(n)$ can be represented by the series expansion $S_2(u) = (\sum_i b_i u^i)^{-1}$ in the domain $0 < u < 1$, and that integrals of the form $\int r^j v_{sym}^{-1} d^3r$ are analytically expressible in terms of a series expansion of integer Fermi integrals:

$$\int \frac{r^j}{v_{sym}} d^3r = 4\pi \rho_o a^{3+j} \left[\frac{F_{2+j}(y)}{S_v} - (2+j) \mathcal{T} F_{1+j}(y) + \dots \right], \quad (42)$$

where \mathcal{T} is given by the series expansion

$$\mathcal{T} = b_1 + 3b_2/2 + 11b_3/6 + 25b_4/12 + 137b_5/60 \dots \quad (43)$$

for any j . Note that $\sum_i b_i = S_v^{-1}$. For example, the conventional density expansion

$$S_2(u) \simeq S_v + \frac{L}{3}(u-1) + \frac{K_{sym}}{18}(u-1)^2 + \dots, \quad (44)$$

keeping just the first three terms in the expansion of S_2^{-1} , leads to

$$\begin{aligned} b_0 &= \frac{1}{S_v} \left[1 + \frac{L}{3S_v} + \left(\frac{L}{3S_v} \right)^2 - \frac{K_{sym}}{18S_v} \right], \\ b_1 &= \frac{1}{3S_v^2} \left(\frac{K_{sym}}{3} - L - \frac{2L^2}{3S_v} \right), \\ b_2 &= \frac{1}{18S_v^2} \left(\frac{2L^2}{S_v} - K_{sym} \right), \end{aligned}$$

$$\mathcal{T} = \frac{1}{3S_v^2} \left[\frac{K_{sym}}{12} - L - \frac{L^2}{6S_v} \right]. \quad (45)$$

The total symmetry energy of a nucleus, neglecting Coulomb effects, now becomes, after expanding the Fermi integrals in powers of y and keeping the first two terms,

$$E_{sym0} = \frac{(N-Z)^2}{H} \simeq AI^2 S_v \left[1 - \frac{3S_v \mathcal{T}}{y} \right]^{-1}. \quad (46)$$

This expression is identical to the liquid droplet model symmetry energy in the same approximation, $E_{sym0} = AI^2 S_v / [1 + S_s A^{-1/3} / S_v]$, if we identify

$$S_s = -\frac{3aS_v^2 \mathcal{T}}{r_o}. \quad (47)$$

This important result is the generalized hydrodynamical model prediction for $S_s(S_2)$. It is essentially the same as the result for S_s established by Steiner et al.[9], which is

$$\frac{S_s}{S_v} \propto \int_0^1 u \left[\frac{S_v}{S_2(u)} - 1 \right] \mathcal{Q}^{-1/2} \frac{du}{u'} \quad (48)$$

We observe that the simple linear approximation $S_2 \simeq S_v + (L/3)(u-1)$ adopted by Ref. [7] implies that $S_s \simeq aL/r_o$.

We note that keeping higher-order terms in y in the expansions of the Fermi integrals would allow determination of curvature and constant contributions to the symmetry energy. The contributions of these terms has not yet been carefully studied.

Other important results stemming from Eq. (42), keeping the lowest-order terms in y , are

$$\begin{aligned} \int \frac{r^j}{v_{sym}} d^3r &\simeq \frac{A}{S_v} \left(\frac{3}{3+j} + \frac{S_s}{S_v} A^{-1/3} \right), \\ H &\simeq \frac{A}{S_v} \left(1 + \frac{S_s}{S_v} A^{-1/3} \right), \\ \alpha_D &\simeq \frac{AR^2}{20S_v} \left(1 + \frac{5}{3} \frac{S_s}{S_v} A^{-1/3} \right), \end{aligned} \quad (49)$$

exactly as anticipated by Equations (13) and (14).

For the neutron skin thicknesses, we use Equations (30), (49) and (33) to find

$$\begin{aligned} R_n - R_p &= \frac{2Ir_o}{3} \frac{S_s}{S_v} \left(1 + \frac{S_s}{S_v} A^{-1/3} \right)^{-1} \times \\ &\times \left[1 - I^2 \left(1 + \frac{S_s}{S_v} A^{-1/3} \right)^{-2} \right]^{-1}, \end{aligned} \quad (50)$$

which is also very similar to the liquid droplet result when Coulomb effects are neglected. Similarly, we find

$$r_{np} \simeq \sqrt{\frac{3}{5}} \frac{2Ir_o}{3\sqrt{1-I^2}} \frac{S_s}{S_v} \left(1 + \frac{S_s}{S_v} A^{-1/3} \right)^{-1}. \quad (51)$$

2.3 Inclusion of Coulomb effects

In nuclei, the charge repulsion among the protons redistributes neutrons and protons and reduces the neutron skin thickness. To take this into account, and to extend the model of [7], we now include a Coulomb contribution $\mathcal{H}_C = n_p V_C / 2$ in the energy density \mathcal{H} , where, in spherical symmetry, the Coulomb potential is

$$V_C(r) = \frac{e^2}{r} \int_0^r n_p(r') d^3r' + \int_r^\infty \frac{e^2}{r'} n_p(r') d^3r'. \quad (52)$$

If the protons are uniformly distributed for $r < R$,

$$V_C = \frac{Ze^2}{R} \left(\frac{3}{2} - \frac{r^2}{2R^2} \right) \quad (53)$$

for $r < R$ and $V_C = Ze^2/r$ for $r > R$. We have found that a reasonable approximation for a Woods-Saxon proton distribution, and one that keeps the model analytic, is provided by assuming Equation (53) to apply for all r . Furthermore, the Coulomb potential and the total Coulomb energy when the Coulomb potential is self-consistently determined are adequately described by the same approximation. Where the discrepancy between this approximation and the real potential is large, the proton density is small. In addition, we will assume that V_C does not significantly alter the total density $n(r)$ so that the relations derived in Equation (49) remain valid whether or not one considers the effects of the Coulomb potential.

For the moment, consider the limit in which the effects of the Coulomb potential on the asymmetry density α are negligible, so that $\alpha = (N-Z)/(v_{sym}H)$. Then, the total Coulomb energy is

$$E_{C0} = \frac{1}{2} \int n_p V_C d^3r = \frac{1}{4} \int n V_C d^3r - \frac{G}{4} \frac{N-Z}{H}, \quad (54)$$

where

$$\begin{aligned} G &= \int \frac{V_C}{v_{sym}} d^3r = \frac{3}{2} \frac{Ze^2}{R} \left(H - \frac{4\alpha_D}{R^2} \right) \\ &= \frac{6}{5} \frac{Ze^2 A}{RS_v} \left(1 + \frac{5}{6} \frac{S_s}{S_v} A^{-1/3} \right). \end{aligned} \quad (55)$$

Assuming that the overall nucleon density n retains the Fermi profile of Equation (37), we find

$$\begin{aligned} E_{C0} &= \frac{Ze^2}{R} \left(\frac{3\pi}{2} n_o a^3 \left[F_2(y) - \frac{a^2}{3R^2} F_4(y) \right] - \right. \\ &\quad \left. - \frac{3}{8} (N-Z) \left[1 - \frac{4\alpha_D}{HR^2} \right] \right) \\ &\simeq \frac{3Z^2 e^2}{5R} \left[1 + \frac{N-Z}{12Z} \frac{S_s A^{-1/3}}{S_v + S_s A^{-1/3}} \right], \end{aligned} \quad (56)$$

where we keep only the lowest order terms in y and so ignore diffuseness corrections. The second term in the brackets of the last line is generally of order 1% of the first term for heavy nuclei, and we therefore find, as expected, that

E_{C0} is essentially the same as in the case of a uniform proton distribution. This indicates that the adopted shape of V_C is relatively unimportant, justifying our approach.

To include the effects of the Coulomb potential on the asymmetry density, we perform the second variation in Equation (19):

$$\alpha = \frac{\bar{\mu} + fV_C/4}{2v_{sym}} = \frac{N - Z - f(G - V_C H)/8}{v_{sym}H}. \quad (57)$$

The factor $f = 1 + \partial \ln V_C / \partial \ln n_p$ depends on whether V_C is assumed to depend on n_p for the purposes of the variational operator $\delta\alpha$. Since the variation of the total energy is done at fixed N and Z , it could be argued that $f = 1$. On the other hand, the definition of V_C (Equation 52) shows it is proportional to n_p , in which case $f = 2$. We will assume $f = 2$ in our subsequent calculations.

We now observe that

$$\begin{aligned} \alpha_o &= \frac{n_o}{S_v H} \left[N - Z - \frac{f}{8} \left(G - \frac{3}{2} H \frac{Z e^2}{R} \right) \right] \\ &= \frac{n_o A}{S_v H} \left[I + \frac{3f}{4} \frac{Z e^2}{R} \frac{\alpha_D}{A R^2} \right], \end{aligned} \quad (58)$$

showing that polarization effects result in an increase in asymmetry near the center of a nucleus, as previously noted by Danielewicz [10].

The total symmetry and Coulomb energy is

$$\begin{aligned} E_{sym} + E_C &= \int v_{sym} \alpha^2 d^3 r + \frac{1}{2} \int n_p V_C d^3 r \\ &\simeq E_{sym0} + E_{C0} + \frac{3f(2-f)}{11200} \frac{Z^2 e^4 A}{R^2 S_v} \times \\ &\times \left(1 + \frac{10S_s}{3S_v} A^{-1/3} \right) \left(1 + \frac{S_s}{S_v} A^{-1/3} \right)^{-1}. \end{aligned} \quad (59)$$

When $f = 2$, the last term vanishes; even if $f = 1$, its magnitude is negligible in comparison to the other terms, being at most 1 MeV, or .1% of the leading terms, for ^{208}Pb . Thus, the total symmetry and Coulomb energy is barely affected by the inclusion of Coulomb potential effects on the distributions of neutrons and protons.

The major role of the Coulomb energy on the symmetry energy correlations arises from the term proportional to $N - Z$ in E_{C0} in Equation (56). We note this term is the same as in the liquid droplet model [9] but is 1/2 the value derived by Danielewicz [10]. This term affects the derived slope of the correlation between L and S_v , which is therefore different from that in Ref. [10]. Given that $I \simeq 0.2$ for typical heavy nuclei, the $N - Z$ term increases the correlation slope dL/dS_v by about 11% in our approach compared to about 25% in Danielewicz's. Steiner et al. [9] noted that Danielewicz's approach (labelled the " μ_α " model) led to an offset and an appreciably steeper correlation than the liquid droplet approach (labelled the " μ_n " model) which are apparently incompatible with Thomas-Fermi and Hartree-Fock fits to nuclear binding energies (such as those found by Refs. [11,12,13]). In spite of the symmetric treatment of neutrons and protons in the " μ_α " approach, which physically seems more justified than the

asymmetric treatment of the liquid droplet approach [8], Ref. [9] was unable to satisfactorily explain this discrepancy. We conclude that the " μ_α " model overestimates the Coulomb modifications to the total energy.

Interestingly, including Coulomb potential effects on the asymmetry in nuclei does not change the dipole polarizability. Applying the dipole constraint, as in Equation (24), one finds

$$\begin{aligned} \alpha_d &= \frac{\epsilon z + fV_C/2}{2v_{sym}}, \\ \alpha_D &= \frac{1}{4\epsilon} \int z \frac{\epsilon z + fV_C/2}{v_{sym}} d^3 r = \frac{1}{12} \int \frac{r^2}{v_{sym}} d^3 r, \end{aligned} \quad (60)$$

where the second term in the middle expression for α_D vanishes because of symmetry.

To examine the role of Coulomb effects on the neutron skin thickness, we now note that

$$\frac{n_n}{n_{no}} - \frac{n_p}{n_{po}} = \frac{2n_o}{n_o^2 - \alpha_o^2} \left[\left(\frac{S_v}{v_{sym}} - n \right) \frac{\alpha_o}{n_o} - \frac{f}{16v_{sym}} \frac{Z e^2}{R} \frac{r^2}{R^2} \right]. \quad (61)$$

The neutron skin thickness when Coulomb effects are included becomes

$$\begin{aligned} \frac{4\pi}{3} (R_n^3 - R_p^3) &= \frac{2n_o}{n_o^2 - \alpha_o^2} \times \\ &\times \left[(S_v H - A) \frac{\alpha_o}{n_o} - \frac{3Z e^2 f}{4R} \frac{d}{R^2} \right], \end{aligned} \quad (62)$$

or

$$\begin{aligned} R_n - R_p &\simeq \frac{2r_o}{3} \left[I \frac{S_s}{S_v} - \frac{3Z e^2 f}{80r_o S_v} \left(1 + \frac{5S_s}{3S_v} A^{-1/3} \right) \right] \times \\ &\left(1 + \frac{S_s}{S_v} A^{-1/3} \right)^{-1} \left[1 - \left(\frac{\alpha_o}{\rho_o} \right)^2 \right]^{-1}. \end{aligned} \quad (63)$$

A related result was found in Ref. [10]:

$$\begin{aligned} R_n - R_p &\simeq \frac{2r_o}{3(1-I^2)} \frac{S_s}{S_v} \left[I - \frac{Z e^2}{20R S_v} \right] \times \\ &\left(1 + \frac{S_s}{S_v} A^{-1/3} + \frac{e^2 A^{2/3}}{80R S_v} \frac{S_s}{S_v} \right)^{-1}. \end{aligned} \quad (64)$$

In both models Coulomb effects reduce the neutron skin thickness for neutron-rich nuclei, and they induce a proton skin in symmetric nuclei. However, the Coulomb effects are much larger within the hydrodynamical model. It is straightforward to see how this leads to a negative correlation between L and S_v . If we approximate $S_s \simeq (a/r_o)L$, and ignore the last term in the denominator of Equation (63), one finds by variation at fixed $R_n - R_p$

$$\begin{aligned} \frac{dL}{L} \left(I - \frac{2}{3} \frac{P}{S_v} A^{-1/3} \right) &\simeq \frac{dS_v}{S_v} \times \\ &\times \left[I - \frac{P}{S_s} \left(1 + \frac{10S_s}{3S_v} A^{-1/3} + \frac{5S_s^2}{3S_v^2} A^{-2/3} \right) \right], \end{aligned} \quad (65)$$

where $P = 3Z e^2 f / (80r_o) \simeq 7.8$ for $f = 2$ and for ^{208}Pb . As long as $S_s/S_v > 0$, the bracket on the second line is

negative and $dL/dS_v < 0$. According to Equation (64), the equivalent expression for the treatment of Ref. [10] is

$$\frac{dL}{L} \left(I - \frac{q}{S_v} \right) \simeq \frac{dS_v}{S_v} \left(I - \frac{2q}{S_v} \right), \quad (66)$$

where $q = Ze^2/(20R) \simeq 0.875$ for ^{208}Pb . Since $I > 2q/S_v$, however, the correlation dL/dS_v is always positive in this approach.

Nevertheless, Coulomb effects contribute to an even greater reduction in the mean-square neutron skin thickness. In the hydrodynamical model with Coulomb effects included, the mean-square radii are

$$\begin{aligned} r_{n,p}^2 &= \frac{1}{2(N, Z)} \int (n \pm \alpha) r^2 d^3r \\ &\simeq \frac{3}{5} \frac{R^2}{1 \pm I} \left[1 \pm I \frac{1 + \frac{5}{3} \frac{S_s}{S_v} A^{-1/3}}{1 + \frac{S_s}{S_v} A^{-1/3}} \right. \\ &\quad \left. \mp \frac{Ze^2 f}{140RS_v} \frac{1 + \frac{10}{3} \frac{S_s}{S_v} A^{-1/3}}{1 + \frac{S_s}{S_v} A^{-1/3}} \right], \end{aligned} \quad (67)$$

where the upper (lower) sign refers to $n(p)$. We then find

$$\begin{aligned} r_{np} &\simeq \sqrt{\frac{3}{5(1-I^2)} \frac{2r_o}{3} \left(1 + \frac{S_s}{S_v} A^{-1/3} \right)^{-1}} \times \\ &\quad \times \left[I \frac{S_s}{S_v} - \frac{3Ze^2 f}{280r_o S_v} \left(1 + \frac{10}{3} \frac{S_s}{S_v} A^{-1/3} \right) \right]. \end{aligned} \quad (68)$$

Note that the coefficient of the last term in the square brackets is 2/7 of that in Equation (63). It is interesting that Ref. [10] obtained a nearly identical result for r_{np} (if $f = 2$ is assumed) in spite of the fact that their results for $R_n - R_p$ and E_{sym0} differ.

If we were to approximate $S_s \simeq aL/r_o$ and ignore the $1 - I^2$ denominator term in Equation (33), then one finds by variation at fixed r_{np} :

$$\begin{aligned} \frac{dL}{L} \left(I - \frac{2}{3} \frac{P}{S_v} A^{-1/3} \right) &\simeq \frac{dS_v}{S_v} \times \\ \times \left[I - \frac{2P}{7S_s} \left(1 + \frac{20S_s}{3S_v} A^{-1/3} + \frac{10S_s^2}{3S_v^2} A^{-2/3} \right) \right], \end{aligned} \quad (69)$$

The correlation dL/dS_v is negative only as long as $S_s/S_v \lesssim 0.6$. However, this result is particularly sensitive to the dependence of S_s on S_v and L , as we now show.

Suppose

$$\begin{aligned} d \ln S_s &= a d \ln L + b d \ln S_v; \\ d \ln r_{np} &= \alpha d \ln S_s - \beta d \ln S_v. \end{aligned} \quad (70)$$

Then, holding r_{np} fixed implies that

$$\frac{d \ln L}{d \ln S_v} = \frac{\beta - b\alpha}{a\alpha}. \quad (71)$$

The skin thickness correlation will be negative if $b > \beta/\alpha$. Lattimer & Lim [2] found that Thomas-Fermi semi-infinite surface calculations of S_s could be approximated by

$$\frac{S_s}{S_v} \simeq 0.6461 + \frac{S_v}{97.85 \text{ MeV}} + 0.4364 \frac{L}{S_v} + 0.0873 \frac{L^2}{S_v^2}. \quad (72)$$

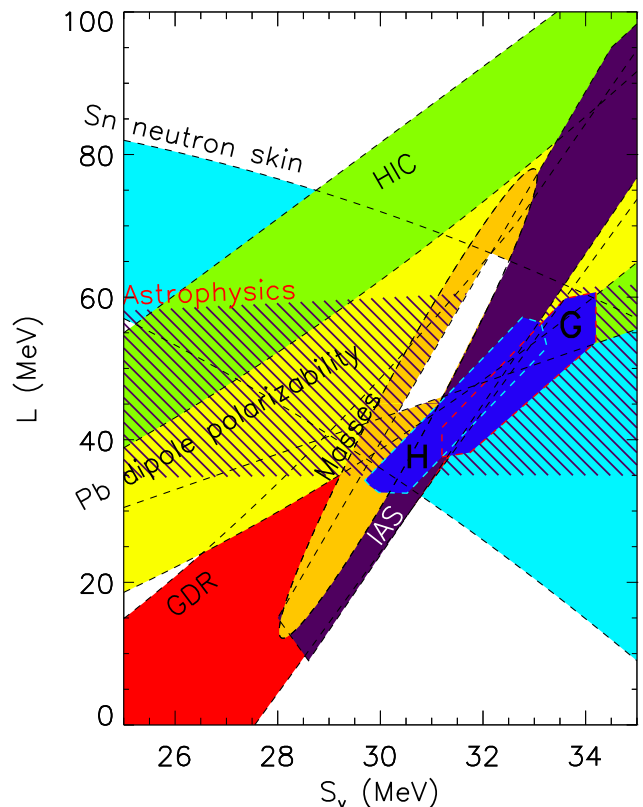


Fig. 1. Experimental constraints for symmetry energy parameters, adapted and revised from [2]. See the text for further discussion. G and H refer to the neutron matter studies of Gandolfi et al. [14] and Hebeler et al. [15], respectively.

Assuming $S_v \simeq 31$ and $L \simeq 45$ MeV, one finds $S_s/S_v \simeq 1.76$, $a \simeq 0.56$, $b \simeq 0.62$, $\alpha \simeq 0.18$ and $\beta \simeq 0.07$, so that $d \ln L/d \ln S_v \simeq -0.4$. It appears that the hydrodynamical model formula, Equation (45), underpredicts both S_s and its dependence on S_v , possibly due to the neglect of cross terms involving gradients of α in Equation (17).

Despite these shortcomings of the model, it allows for a qualitative understanding of the role of the symmetry energy in nuclear properties and for the correlations between S_v and L that have been observed. In particular, it demonstrates that a precision measurement of the neutron skin thickness is extremely important because its implied correlation between S_v and L is essentially orthogonal to those provided by fitting nuclear masses and measuring dipole excitation energies.

2.4 Comparison with experimental data

It is now useful to compare experimental results for binding energies, neutron skin thicknesses, dipole polarizabilities, and centroids of giant dipole resonances. These were recently reviewed in Ref. [2] and we summarize the results in Fig. 1.

The correlation between L and S_v for measured nuclear masses is taken from Hartree-Fock calculations with

the UNEDF0 density functional[11], in which the nominal fitting error was arbitrarily chosen to be $\sigma = 2$ MeV. In all likelihood, this value is overestimated, as negative values for L , which give negative neutron matter pressures, are reached. As a result, the confidence ellipse is probably smaller than given in Ref. [11] and we have instead chosen the value $\sigma = 1$ MeV. Importantly, the shape and orientation of the ellipse are the same as predicted by the liquid droplet model, Eq. (13), once the dependence of S_s on S_v and L is taken into account.

The constraints for the neutron skin thickness of ^{208}Pb are taken from a study by Chen et al. [16], who converted the experimental results[17, 18, 19, 20, 21, 22] for Sn isotopes into an equivalent value for ^{208}Pb : $r_{np} \simeq (0.175 \pm 0.020)$ fm. Performing a series of Skyrme Hartree-Fock calculations of ^{208}Pb , in which values of S_v and L were systematically varied, they also established that

$$\frac{r_{np}}{\text{fm}} \simeq -0.094669 + \frac{7.2028S_v}{\text{GeV}} + \frac{2.3107L}{\text{GeV}} - \frac{8.8453S_v^2}{\text{GeV}^2} - \frac{47.837S_vL}{\text{GeV}^2} + \frac{4.003L^2}{\text{GeV}^2}. \quad (73)$$

This formula, with the aforementioned value for r_{np} , establishes the correlation slope $d \ln L / d \ln S_v \simeq -3.75$, assuming $S_v = 31$ MeV and $L = 45$ MeV. This result is somewhat steeper than the slope predicted by the hydrodynamical model (which is essentially flat), and it should be explored with a greater variety of effective interactions.

Similarly, the constraint for the electric dipole polarizability α_D of ^{208}Pb is taken from data produced by Tamii et al. [23]: $\alpha_D \simeq (20.1 \pm 0.6)$ fm³. Roca-Maza et al. [24] showed, from studies with a series of relativistic and non-relativistic interactions, that the dipole polarizability, bulk symmetry parameter, and the neutron skin thickness for ^{208}Pb can be constrained by

$$\alpha_D S_v \simeq (325 \pm 14) + (1799 \pm 70)(r_{np}/\text{fm}) \text{ MeV fm}^3. \quad (74)$$

By use of Equation (73), this is converted onto the $S_v - L$ correlation shown in Figure 1.

Equation (74) is not functionally the same as that established from the hydrodynamical model, whose dependence on S_v and S_s can be gleaned from Equations (60) and (68). Although the predicted slopes of both correlations are similar, being positive and somewhat less steep than that from nuclear masses, the functional difference suggests that the correlation of Ref. [24] might retain some model-dependence and should be further explored. Note that the slope of this correlation is significantly different than shown in [2], which relied on the analysis in Ref. [25] that erroneously concluded $\alpha_D \propto r_{np}$.

The constraint for the centroid energy of the giant dipole resonance for ^{208}Pb is taken from Trippa, Coló and Vigezzi [26]. They concluded that the measured energy was best fit by those forces having a bulk symmetry energy $S_2(0.1)$, evaluated at the density $n = 0.1$ fm⁻³, in the range $S_2(0.1) \simeq (24.1 \pm 0.9)$ MeV. This symmetry energy value can be converted into a correlation between S_v and L for a given nuclear force model. Lattimer & Lim [2] deduced the band shown in Figure 1 by studying a wide

range of plausible density functionals. Unfortunately, the hydrodynamical model does not yield an analytic prescription for this correlation, but one should expect it to be similar to that of the dipole polarizability, which is borne out by the results shown in Figure 1.

Additional correlations depicted in Figure 1 are due to studies of isospin diffusion in heavy-ion collisions [27] and energies of excitations to isobaric analog states [28]. The model-dependence of the former analysis has not been fully explored, although the depicted results are consistent with multifragmentation studies in intermediate-energy heavy ion collisions [29] which imply $40 \text{ MeV} < L < 125 \text{ MeV}$. Excitation energies are sensitive to shell effects, but are closely related to the energies of nuclear ground states. Thus, the latter correlation bears a great deal of resemblance to that determined from nuclear binding energies. Danielewicz & Lee also utilized measurements[17, 30, 31, 32, 33] of the ^{208}Pb skin thickness to further restrict the allowed $S_v - L$ parameter space. The weighted average of neutron skin thicknesses they employed was $r_{np} = (0.179 \pm 0.023)$ fm, 0.004 fm larger than determined by Ref. [16] and used in Fig. 1. Their combined analysis of isobaric analog states and skin thickness measurements result in the restriction $33 \text{ MeV} < L < 72 \text{ MeV}$ (not shown in Fig. 1).

In contrast, the white region displayed in Fig. 1 represents the consensus agreement of the six experimental constraints we have discussed, giving a somewhat smaller range $44 \text{ MeV} < L < 66 \text{ MeV}$. (In comparison to the consensus region found in Ref. [2], the region displayed in Fig. 1 is slightly smaller because of the incorporation of the additional constraint from isobaric analog states.) Since the model dependencies of these constraints have not been thoroughly explored, the size of this consensus region may well be underestimated. If we treat the white region as a 68% confidence interval for the experimental determination of S_v and L , it can be used with Monte Carlo sampling to determine a distribution of neutron star matter pressures by means of Eq. (7). This can then be combined with further Monte Carlo sampling of Eq. (8), whose uncertainty reflects one standard deviation, to determine the confidence interval for radii of $1.4M_\odot$ stars: $R_{1.4} \simeq (12.1 \pm 1.1)$ km to 90% confidence. (Employing the r_{np} constraint of Ref. [28] instead of Ref. [16], the upper limit to L increases to about 69 MeV and the lower and upper limits to r_{np} increase by about 0.1 km.) As we will see, this range is quite compatible with several astrophysical observations.

2.5 Neutron matter studies

Two recent studies of pure neutron matter using realistic two- and three-nucleon interactions coupled with low-energy scattering phase shift data, the first employing chiral Lagrangian methods [15] and the second using quantum Monte Carlo techniques [14], can also render constraints on symmetry energy coefficients and neutron star radii [34, 35]. With the important assumption that higher-than-quadratic terms in Eq. (2) are ignored, the values of

the neutron matter energy and pressure at n_s provide direct estimates of S_v and L . The estimated error ranges for the symmetry parameters determined [15] from neutron matter studies are also displayed in Fig. 1. These estimates are very consistent with those determined from nuclear experiments, but their small displacement may represent the effects of neglecting quartic or higher-order terms in the symmetry energy expansion.

3 Estimates of Neutron Star Radii

Although nearly three dozen neutron star masses have been determined very accurately [36], there are no precise simultaneous measurements of a star’s mass and radius. To date, several different astrophysical measurements of neutron star radii have been attempted. We will focus attention on radius estimates inferred from photospheric radius expansion (PRE) bursts and thermal emissions from quiescent low-mass X-ray binaries (QLMXBs) and isolated neutron stars. Unfortunately, no single observation, at the present time, can reliably determine a neutron star radius to better than 20% accuracy. This translates into nearly a 100% error for the determination of L , since $L \propto R^4$ using Equations (7) and (8), which is substantially larger than the accuracy afforded by nuclear experiments and neutron matter theory [2]. Moreover, with such large errors in M and R for an individual source, the direct inversion of the neutron star structure equations cannot credibly limit the pressure-density relation.

Even taking the ensemble of measurements and attempting to invert the neutron star structure equations to infer the $M - R$ relation is problematic without physical guidance. How does one choose the weighting for a particular EOS and $M - R$ curve: does one place more emphasis on its passing close to the central values of the measurements, or does one integrate the effective weight along the entire $M - R$ curve? Fortunately, Bayesian techniques make it clear how to add integrate the weight along the curve. The body of observations can be coupled to the structure equations, as shown by [37], to effectively determine the $M - R$ relation and, further, to obtain estimates of the pressure-density relation of neutron star matter, not only near ρ_s , but up to the highest densities found in neutron star interiors. Relative estimated errors of the pressure of high-density matter can be as large as 150% but are generally much smaller. The final results and model comparisons are given in §4 and discussed in §5.

The nuclear symmetry energy is also connected to other outstanding problems in nuclear astrophysics, including the crustal properties of neutron stars, the possible onset of the direct Urca process at high densities in the neutron star interior, and the quark-hadron transition and the appearance of other exotica such as hyperons and meson condensates.

3.1 Photospheric Radius Expansion Bursts

Accretion onto neutron stars in binaries often leads to X-ray bursts from the unstable burning of the accreted ma-

terial from its companion. The nuclear burning spreads across the stellar surface and gives rise to a sudden increase in X-ray luminosity and temperature. Some of these X-ray bursts are energetic enough to reach the so-called Eddington limit at which radiation pressure is sufficiently large to overcome gravity, leading to expansion of the star’s photosphere. These PRE bursts can constrain M and R because the largest flux during the burst must be near the Eddington flux

$$F_{\text{Edd}} = \frac{cGM}{\kappa R^2} (1+z) \quad (75)$$

where $z = (1-2\beta)^{-1/2} - 1$ is the redshift of the source and $\beta = GM/Rc^2$ is the dimensionless compactness parameter. The observed Eddington flux is diluted by distance and is twice redshifted (once for energy, once for time):

$$F_{\text{Edd},\infty} = \frac{cGM}{\kappa D^2} (1+z)^{-1}. \quad (76)$$

It has been usually assumed that the flux measured when the effective temperature is a maximum corresponds to the Eddington flux and that “touchdown” has occurred, i.e., the photosphere is coincident with R [38]. If this is the case, the appropriate redshift to be applied is as given above. If the maximum temperature point is reached while the photosphere is above the stellar surface, the effective redshift might actually be negligible. In any case, measurement of the peak flux (or Eddington flux) constitutes an observable which is a function of M, κ, D , and possibly R . The reproducibility of the maximum flux from repeated energetic bursts from the same source supports the identification of this flux with the Eddington limit.

A second observable in these systems is the nearly constant angular emitting area during the cooling tail several seconds after the burst’s peak. The emission is nearly thermal, and simultaneous measurement of the observed (redshifted) flux and (redshifted) temperature can yield an angular diameter if the effects of the atmosphere, through the color correction factor $f_c = T_c/T_{\text{eff}}$ between effective temperature and color temperature, are known:

$$A \equiv \frac{F_\infty}{\sigma T_{\text{eff},\infty}^4} = f_c^{-4} \left(\frac{R_\infty}{D} \right)^2, \quad (77)$$

where $R_\infty = R(1+z)$ is the apparent radiation radius and $T_{\text{eff},\infty} = T/(1+z)$ is the observed effective temperature. Repeated bursts from the same source show the same emitting areas, suggesting strongly that the entire neutron star surface is emitting during the cooling tail and that non-spherically symmetric effects during this phase are small. The observable A is thus a function of M, R, f_c and D . With knowledge of D, f_c and κ , the mass and radius can be deduced from $F_{\text{Edd},\infty}$ and A .

The observables $F_{\text{Edd},\infty}$ and A can be combined into two parameters,

$$\alpha = \frac{F_{\text{Edd},\infty}}{\sqrt{A}} \frac{\kappa D}{f_c^2 c^3} = \beta(1-2\beta),$$

$$\gamma = \frac{A}{F_{\text{Edd},\infty}} \frac{f_c^4 c^3}{\kappa} = \frac{R}{\beta(1-2\beta)^{3/2}}, \quad (78)$$

where we used Equation (76) to establish the second set of equalities. These, in turn, can be solved for M and R :

$$\beta = \frac{1}{4} \pm \frac{1}{4} \sqrt{1-8\alpha},$$

$$R = \alpha\gamma\sqrt{1-2\beta}, \quad M = \alpha^{3/2}\gamma\beta^{1/2}c^2/G. \quad (79)$$

Note that γ is independent of D and $R_\infty = \alpha\gamma$ is independent of κ and $F_{\text{Edd},\infty}$. For real solutions to exist, α must be less than or equal to $1/8$. However, we shall see that observations imply this condition is usually not met.

To date, five PRE X-ray bursters have been studied by Özel and collaborators. We collect results for D , $F_{\text{Edd},\infty}$ and A for each source in table 2. Uncertainties for these quantities are assumed to be Gaussian with the indicated 1σ error bars. Values of α and γ can be found with additional assumptions for κ and f_c . The opacity in these high-temperature sources is dominated by electron scattering, and we employ the Thomson opacity $\kappa = 0.200m_B^{-1}(1+X)$ $\text{cm}^2 \text{g}^{-1}$, where m_B is the baryon mass and $0 < X < 0.7$ is the mass fraction of hydrogen. This range for X reflects the uncertainty in compositions which could range from pure He at one extreme to solar at the other. Also, following [37], we assume that $f_c = 1.40 \pm 0.07$, a slightly larger range than Özel et al. have assumed. The uncertainty distributions for κ and f_c are taken to be boxcar shaped. The computed values for α and γ reflect the combined uncertainties of observables and physical parameters using Monte Carlo sampling.

It is clear from table 2 that none of the sources satisfy $\alpha \leq 1/8$ to within 1σ . If the observed quantities $F_{\text{Edd},\infty}$, D and A are Monte Carlo sampled within their probability distributions, nearly all the resulting values of α will be greater than $1/8$ and those trials must be rejected. Those trials that will be accepted will cluster near $\alpha = 1/8$, which is more easily accomplished if $X \simeq 0$ and $f_c \simeq 1.47$. The fraction of accepted trials are shown in the last column of table 3. In turn, accepted γ values will be near the upper end of the ranges given in table 2. As a consequence, in this model, $\alpha \simeq 1/8$ to within 1σ , irrespective of the values of the observables, as can be seen in table 3. Also, the error bars of the derived quantities are seen to be artificially reduced in this case, which does not seem justified. The probability distributions for inferred values of R and M are shown in Figure 2, which shows that the distributions are bimodal with each lobe carrying equal total weight. The average values listed in table 2 are intermediate between the two probability clumps. Note that the distributions computed by Refs. [39,40,41] are incorrect, but were corrected by Ref. [44].

Sources of systematic uncertainties not accounted for in this simple model are possible asymmetries in emission as well as the assumption that the photosphere is at the neutron star surface when $F_{\text{Edd},\infty}$ is measured. Steiner et al. [37] attempted to include these uncertainties by allowing the effective redshift of the photosphere, z_{ph} , to be randomly chosen from a distribution uniformly populated

with $1/(1+z_{\text{ph}})^2$ between 0 and $1/(1+z)^2$. In the extreme case that $z_{\text{ph}} = 0$, Equation 78 becomes

$$\alpha = \frac{F_{\text{Edd},\infty}}{\sqrt{A}} \frac{\kappa D}{f_c^2 c^3} = \beta\sqrt{1-2\beta},$$

$$\gamma = \frac{A}{F_{\text{Edd},\infty}} \frac{f_c^4 c^3}{\kappa} = \frac{R}{\beta(1-2\beta)}. \quad (80)$$

Solving these for M and R yields a new set of relations:

$$\beta = \left[1 + \sqrt{3} \sin(\theta/3) - \cos(\theta/3) \right] / 6,$$

$$R = \alpha\gamma\sqrt{1-2\beta}, \quad M = \alpha^2\gamma c^2/G, \quad (81)$$

where $\theta = \cos^{-1}(1-54\alpha^2)$. When $\alpha < 3^{-3/2} \simeq 0.192$, θ is real and there are 3 real roots for β . One of these is negative, and another is greater than $1/3$ which nearly violates the causality constraint for neutron stars[1]. The remaining real root is the one given in Equation (81). When $\alpha > 3^{-3/2}$, θ and all roots for β are imaginary. Table 2 indicates that, to within 1σ , all five sources have $\alpha < 0.192$, so that Monte Carlo sampling of the observables within their probability distributions should yield a much larger fraction of physically acceptable solutions. Indeed, this is borne out by the acceptance fraction shown in table 3. Accepting only those trials for which $\alpha < 0.192$, table 3 shows averages and standard deviations for M and R under the assumption that $z_{\text{ph}} = 0$. Interestingly, values of α are larger and values of γ are smaller than in the previous case, with the consequence that in three of the five cases the values of $R_\infty = \alpha\gamma$ are largely unchanged. The uncertainty ranges are much less compressed compared to the case $z_{\text{ph}} = z$, and derived values of R are on average 1.2 km larger. While the high percentage of accepted trials with $z_{\text{ph}} = 0$ is encouraging, this model remains oversimplified and the possibility that $z_{\text{ph}} = z$ cannot be ruled out. The average neutron star mass and radius implied by these results are $\bar{R} = 10.77 \pm 0.65$ km and $\bar{M} = 1.65 \pm 0.12M_\odot$, and the probability distributions are displayed in Figure 3. Given expectations that neutron star radii don't change much with neutron star mass, these relatively small standard deviations are interesting.

3.2 Quiescent Low-Mass X-ray Binaries

Certain neutron stars in binary systems may intermittently accrete matter from an evolving companion star, with episodes of accretion separated by long periods of quiescence. While the neutron star accretes, compression of matter in the crust induces nuclear reactions that release heat in sufficient amounts to warm the star to temperatures not seen since its birth, these neutron stars cool via neutrino radiation from their interiors and X-rays from their surfaces. It is generally believed that accretion suppresses surface magnetic fields, which is an advantage of using these systems for radius measurements compared to isolated neutron stars for which strong, uncertain, magnetic fields may exist. Strong magnetic fields can significantly affect a star's atmosphere and introduce large uncertainties in radius measurements. In addition, due to the

Table 2. PRE X-ray bursters and estimated Eddington fluxes, angular areas and distances taken from the indicated references. Values and uncertainties for α , γ and R_∞ reflect assumptions about f_c and X as discussed in the text.

PRE Source	D kpc	$F_{\text{Edd},\infty}$ 10^{-8} erg cm $^{-3}$ s $^{-1}$	A km 2 kpc $^{-2}$	α	γ km	R_∞ km
EXO 1745-248[39]	6.3 ± 0.6	6.25 ± 0.2	1.17 ± 0.13	0.188 ± 0.035	76.86 ± 17.33	14.57 ± 1.64
4U 1608-522[40]	5.8 ± 1.0	15.41 ± 0.65	3.246 ± 0.024	0.247 ± 0.058	90.22 ± 17.09	20.36 ± 3.68
4U 1820-30[41]	8.2 ± 0.7	5.39 ± 0.12	0.9198 ± 0.0186	0.235 ± 0.041	69.16 ± 13.62	15.82 ± 1.58
KS 1731-260[42]	8.0 ± 0.4	4.45 ± 0.12	0.884 ± 0.051	0.199 ± 0.032	82.79 ± 16.57	15.63 ± 1.18
SAX J1748.9-2021[43]	8.2 ± 0.6	4.03 ± 0.44	0.897 ± 0.096	0.177 ± 0.036	97.64 ± 23.08	15.74 ± 1.61

Table 3. PRE X-ray burster solutions resulting from Monte Carlo trials with parameters taken from their uncertainty intervals. Only solutions with real values of R are accepted; the fraction of Monte Carlo acceptances is shown in the last column.

PRE Source	α	γ km	R_∞ km	R km	M M_\odot	acceptance %
$z_{\text{ph}} = z$						
EXO 1745-248	0.117 ± 0.006	109.0 ± 14.2	12.77 ± 1.62	9.11 ± 1.55	1.45 ± 0.28	4.87
4U 1608-522	0.115 ± 0.010	110.8 ± 16.4	12.73 ± 2.22	9.21 ± 1.74	1.41 ± 0.38	0.861
4U 1820-30	0.121 ± 0.004	103.4 ± 7.5	12.48 ± 0.96	8.81 ± 1.04	1.46 ± 0.19	0.0311
KS 1731-260	0.121 ± 0.004	124.5 ± 9.0	15.01 ± 1.03	10.58 ± 1.23	1.76 ± 0.21	1.01
SAX J1748.9-2021	0.116 ± 0.008	132.9 ± 17.4	15.27 ± 1.65	11.05 ± 1.86	1.69 ± 0.33	9.67
$z_{\text{ph}} = 0$						
EXO 1745-248	0.158 ± 0.021	85.35 ± 15.55	13.25 ± 1.67	10.00 ± 1.45	1.42 ± 0.27	66.3
4U 1608-522	0.167 ± 0.020	103.5 ± 16.2	17.20 ± 3.08	12.41 ± 1.98	1.96 ± 0.49	20.7
4U 1820-30	0.173 ± 0.014	87.04 ± 10.39	15.03 ± 1.58	10.63 ± 1.25	1.77 ± 0.25	24.5
KS 1731-260	0.163 ± 0.018	92.29 ± 13.68	14.87 ± 1.21	11.01 ± 1.28	1.64 ± 0.22	59.2
SAX J1748.9-2021	0.154 ± 0.023	102.1 ± 20.7	15.26 ± 1.64	11.70 ± 1.61	1.58 ± 0.30	72.9

rapid gravitational settling timescales (of order seconds), only the lightest element in accreted matter remains in its atmosphere. Thus, these transient X-ray sources, also known as QLMXBs, are believed to have low-magnetic field H or He atmospheres. The emitted X-ray spectra, for a given composition, will depend largely on R and T_{eff} , and, to a lesser extent, on gravity $g = GM(1+z)/R^2$.

In contrast, the observed spectrum will depend on the distance D and on the amount of interstellar absorption between the source and the observer, usually parameterized by N_H , the column density of H. The absorption is important, as it has an energy dependence of $E^{-8/3}$ and can significantly reduce the observed flux near the peak and at lower energies. It is often difficult to determine distances to field sources, while distance determinations of globular clusters are relatively accurate. For this reason, attention has been focused on systems in globular clusters.

Fitting the observed spectrum in principle can provide estimates for R_∞ , $T_{\text{eff},\infty}$, g and N_H , but due to lack of resolution and poor statistics, the deduced N_H is often at odds with the amount of absorption deduced from HI radio surveys. Although it is obvious that an underestimate of absorption will lead to an underestimate of mass and radius, because decreasing the absorption has a similar effect to decreasing the distance, it is possible through analytic considerations to predict the magnitude

of the effect. For simplification, we first consider the case of a blackbody emitter. The observed energy dependence of the flux from an absorbed blackbody with an effective temperature T obeys

$$F(E, T, N_H) = \alpha E^3 \frac{e^{-bN_{H21}/E^{8/3}}}{e^{E/kT} - 1}, \quad (82)$$

where α is a constant and $b \simeq 0.16$ keV $^{8/3}$ represents the approximate effects of absorption [45]. N_{H21} is the hydrogen column density in units of 10^{21} cm $^{-2}$.

For a given T , the maximum flux occurs at E_0 where $dF/dE = 0$, or

$$E_0 = \left[3 + (8/3)bN_{H21}E_0^{-8/3} \right] \left(1 - e^{-E_0/kT} \right) kT. \quad (83)$$

Therefore $E_0 > 3kT$ in general, and the exponential term is small. The observed flux, neglecting gravity and redshift, is

$$\left(\frac{R}{D} \right)^2 \int_{E_L}^{E_U} F(E, T, N_H) dE, \quad (84)$$

where $E_L \sim 0.3$ keV and $E_H \sim 10$ keV represent the low- and high-energy cutoffs of the X-ray detector response. To compare the effect of changing the amount of absorption on the inferred radius, we assume that both the total observed flux and the peak energy E_0 are held fixed as N_H is

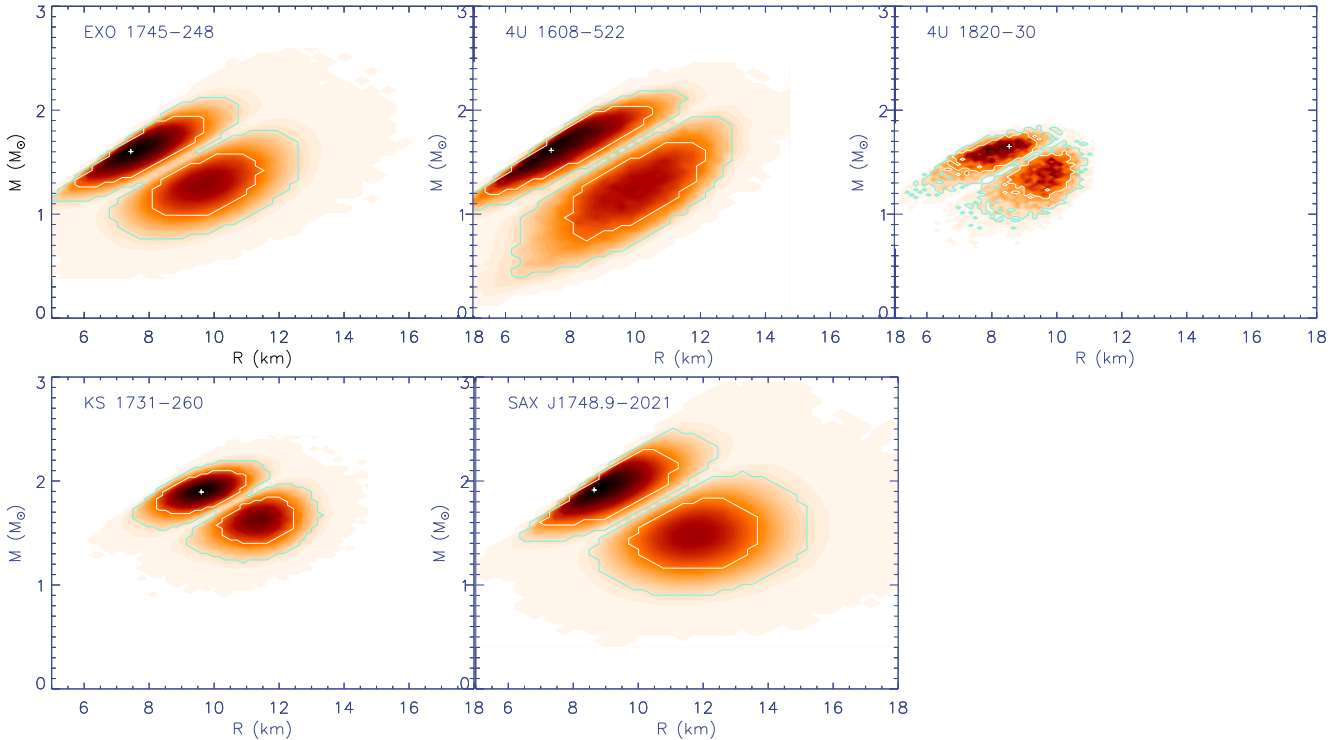


Fig. 2. $M - R$ probability contours for PRE X-ray burst sources assuming that $z_{\text{ph}} = z$. Crosses indicate maximum probabilities and white (green) contours show 1σ (2σ) uncertainty contours.

varied. Changing the H column density from $N_1 = N_{1,H21}$ to $N_2 = N_{2,H21}$ will alter the effective temperature from T_1 to T_2 :

$$\frac{T_2}{T_1} \simeq \frac{9E_0^{8/3} + 8bN_1}{9E_0^{8/3} + 8bN_2}, \quad (85)$$

neglecting the exponential term in Equation 83. Thus, the effective temperature will decrease with an increase in absorption. The ratio of deduced radii follows from Equation 84:

$$\left(\frac{R_2}{R_1}\right)^2 = \frac{\int_{E_L}^{E_U} F(E, T_1, N_1) dE}{\int_{E_L}^{E_U} F(E, T_2, N_2) dE}. \quad (86)$$

These integrals can be approximated by the method of steepest descents to high accuracy: the integration limits are extended to $-\infty$ and ∞ and the integrand is replaced by a Gaussian centered at E_0 . These approximations yield

$$\left(\frac{R_2}{R_1}\right)^2 \simeq \frac{F_1}{F_2} \sqrt{\frac{F_2'' F_1}{F_2 F_1''}}, \quad (87)$$

where $F_1 = F(E_0, T_1, N_1)$ and $''$ indicates a second derivative evaluated at E_0 . One has

$$\frac{F_1}{F_2} \simeq \exp\left[\frac{11b(N_2 - N_1)}{3E_0^{8/3}}\right],$$

$$\frac{F_2'' F_1}{F_2 F_1''} \simeq \frac{27E_0^{8/3} + 88bN_2}{27E_0^{8/3} + 88bN_1}. \quad (88)$$

An increase in N_H necessarily leads to an increase in R since both factors in Equation (88) are greater than unity. For example, for $T_1 = 0.10$ keV, $N_1 = 0.9$ and $N_2 = 1.8$, one finds $E_0 \simeq 0.52$ keV, $T_2 \simeq 0.07$ keV, and $R_2/R_1 \simeq 5.35$. The analytic expressions in Equations (87) and (88) are accurate in this case to better than 1%, compared to the exact integrations of Equation (86) and differentiations of Equation (82). For comparison, Guillot et al. [46] find a ratio $R_2/R_1 \simeq 2$ for similar conditions using an H atmosphere in the case of a source in ω Cen.

The radius change overestimate in the case of a blackbody can be understood using a simple approximation to the shape of the spectrum from an H atmosphere. Following Lattimer & Steiner [47], a hydrogen atmosphere can be approximated by

$$F(E, T, N_H) \simeq \alpha' E^3 \frac{e^{-bN_{H21}/E^{8/3}}}{e^{\beta(E/kT)^p} - 1} \quad (89)$$

where α' depends weakly on T , approximately as $T^{0.2}$, $\beta \simeq 1.35$ and $p \simeq 5/7$. The value of p is a consequence of the dominance of electron scattering in H atmospheres, for which the cross section varies as E^{-3} . Including the effects of absorption, the peak in the observed spectrum

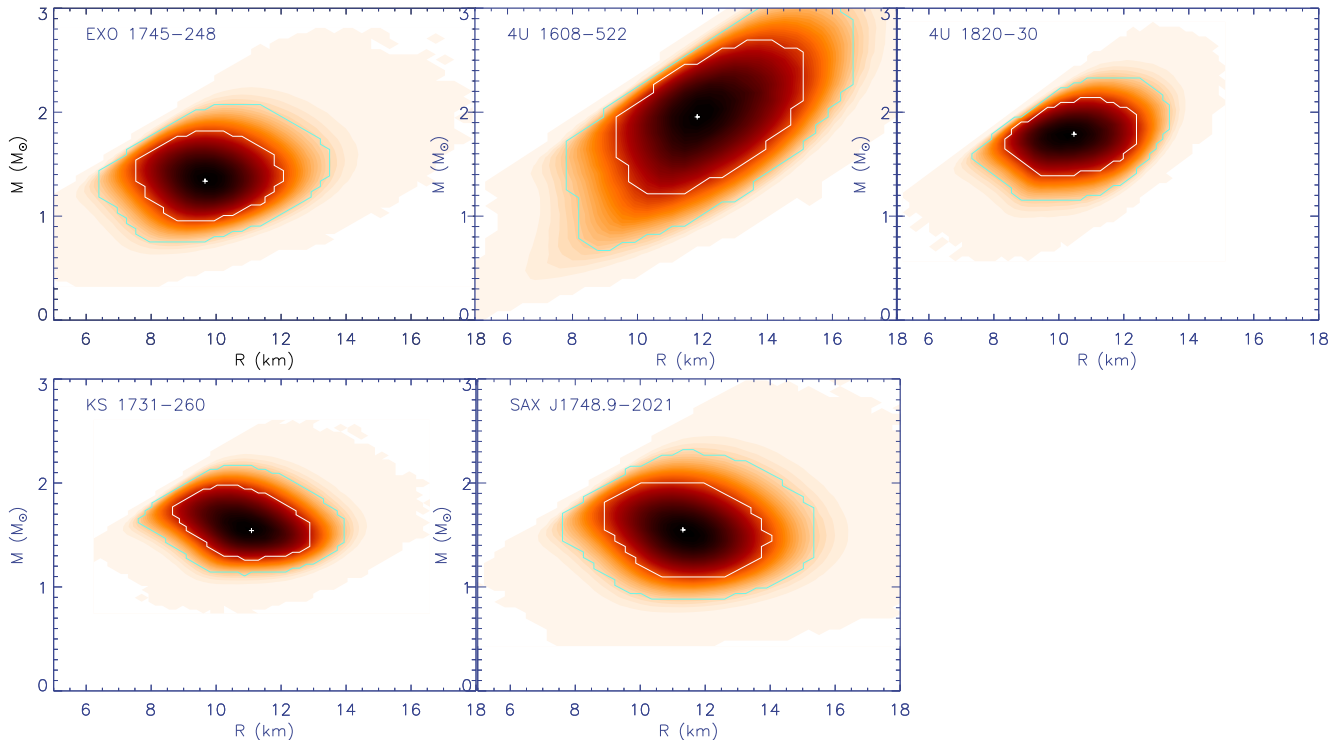


Fig. 3. The same as Figure 2 except assuming that $z_{\text{ph}} = 0$.

occurs when

$$E_0 \simeq \left(\frac{9 + 8bN_{H21}E_0^{-8/3}}{3\beta p} \right)^{1/p} kT, \quad (90)$$

again ignoring the small exponential term. Unabsorbed spectra have an energy peak at $E_0/(kT) \simeq (3/\beta p)^{1/p} \simeq 4.9$, and absorption only makes this factor larger, justifying this approximation. Keeping the peak energy fixed, two different column densities lead to temperatures

$$\frac{T_2}{T_1} \simeq \left(\frac{9E_0^{8/3} + 8bN_1}{9E_0^{8/3} + 8bN_2} \right)^{1/p}. \quad (91)$$

The ratio of inferred radii can be found using

$$\frac{F_1}{F_2} \simeq \left(\frac{T_1}{T_2} \right)^{0.2} \exp \left[\left(\frac{8}{3p} + 1 \right) b \frac{N_2 - N_1}{E_0^{8/3}} \right], \quad (92)$$

$$\frac{F_2'' F_1}{F_2 F_1''} \simeq \frac{27pE_0^{8/3} + 8bN_2(8 + 3p)}{27pE_0^{8/3} + 8bN_1(8 + 3p)}.$$

For the same conditions as previously, one finds $R_2/R_1 \simeq 2.24$, in closer agreement with realistic atmospheres. The relative increase in radius with increasing absorption is very temperature sensitive: it is more pronounced for smaller temperatures, as can be seen in Figure 4.

It is also interesting to explore helium atmospheres, which could be relevant in the case of ultracompact binaries in which the companion is a white dwarf. As in H atmospheres, one expects electron scattering to dominate, especially at higher temperatures. Ref. [47] found that the predicted spectrum of He atmospheres is similar to that of H atmospheres, with $p \simeq 5/7$, but with the value of $\beta \simeq 1.24$ instead of 1.35. Thus, the inferred temperature of a He atmosphere is about 13% less than that of an H atmosphere, and the inferred radius is about 28% larger, assuming that E_0 is unchanged.

In order to estimate the gravity and/or redshift of the atmosphere from the observed spectrum, it is required that an additional aspect of the atmosphere that is sensitive to g and/or z as well as T_{eff} and R , in addition to the peak energy and the overall flux, be measured.

Guillot et al. [46] recently summarized the observed properties of 5 QLMXBs with known distances and modeled them with H atmospheres to derive masses, radii and H column densities. Their results are shown in table 4 and in Figure 5. The most striking feature in these results is that the optimum inferred values of R_∞ range from 8.4 to 23.0 km, of R from 6.4 to 19.4 km, and of M from 1.25 to 2.69 M_\odot . Such large variations are not expected from evolutionary considerations for a relatively uniform class of sources.

Guillot et al. [46] noted that in the most extreme cases of large and small radii (the sources in ω Cen and NGC

Table 4. Inferred properties of QLMXBs

Source	D (kpc)	Guillot et al. (2013)			Lattimer & Steiner (2013)		
		N_{H21}	R_∞ (km)	z	N_{H21}	R_∞ (km)	z
M28	5.5 ± 0.3	2.52	$12.84^{+1.50}_{-1.48}$	$0.198^{+0.485}_{-0.120}$	1.89	$10.65^{+1.27}_{-1.14}$	$0.212^{+0.456}_{-0.123}$
NGC 6397	2.02 ± 0.18	0.96	$8.42^{+1.32}_{-1.36}$	$0.242^{+0.278}_{-0.106}$	1.4	$11.66^{+1.94}_{-1.72}$	$0.241^{+0.279}_{-0.102}$
M13	6.5 ± 0.6	0.08	$11.48^{+2.54}_{-2.29}$	$0.308^{+0.376}_{-0.212}$	0.145	$12.93^{+2.91}_{-2.53}$	$0.286^{+0.392}_{-0.190}$
ω Cen	4.8 ± 0.3	1.82	$23.03^{+4.48}_{-3.86}$	$0.187^{+0.492}_{-0.144}$	1.04	$13.25^{+2.57}_{-2.08}$	$0.200^{+0.456}_{-0.134}$
NGC 6304	6.22 ± 0.026	3.46	$11.52^{+2.73}_{-2.10}$	$0.212^{+0.467}_{-0.120}$	2.66	$9.39^{+2.09}_{-1.75}$	$0.212^{+0.407}_{-0.108}$

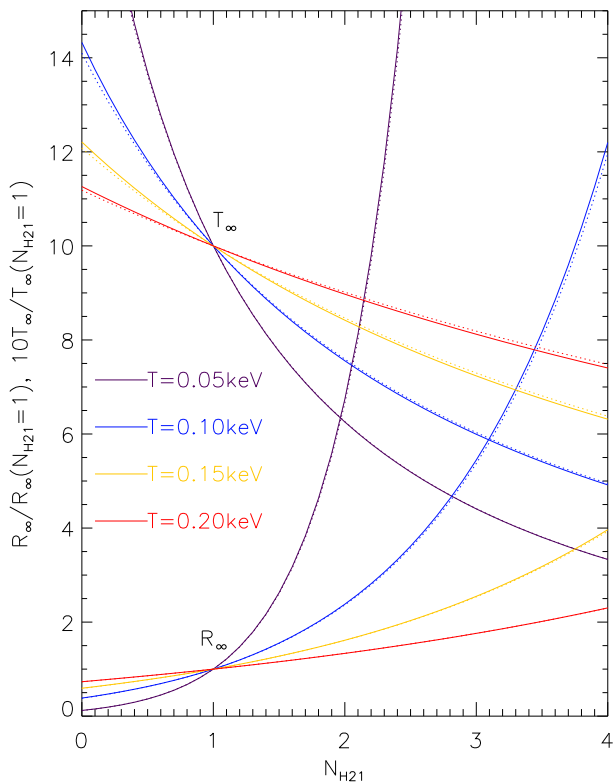


Fig. 4. Relative radii (lower curves) and effective temperatures (upper curves) for H atmospheres as functions of H column densities. Results are shown as ratios relative to the values obtained for the indicated base effective temperature and column density ($N_{H21} = 1.0$). Solid lines show full integrations while dotted lines are the analytic expressions derived from steepest descent integration described in the text.

6397, respectively), the values of N_H they inferred were markedly different from those independently determined [48] by observations of HI column densities in the directions toward the respective globular clusters. Lattimer & Steiner [47] observed, furthermore, that these differences in N_H values acted in such a way as to enhance the disparity of inferred radii found by [46]. Using an analytic

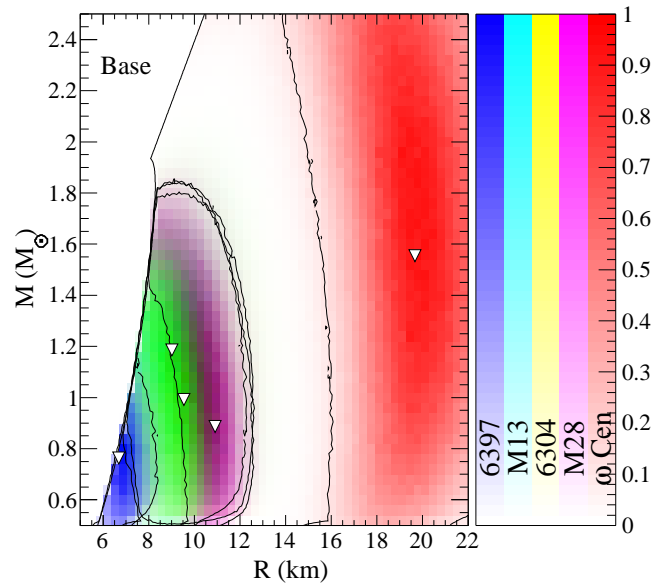


Fig. 5. Probability distributions in M and R for the 5 QLMXBs studied by Guillot et al. [46] in which N_H values are fit to the observed spectra. Color coding for the relative probabilities are indicated by the bar graphs on the right, which are ordered according to their most probable radii (marked by triangles). Solid curves denote 90% confidence boundaries. The left-most curve bounds the region permitted by general relativity, causality, and the observation of a $2M_\odot$ neutron star [47].

procedure as described above, Ref. [47] estimated new values of R_∞ using the alternate N_H values from Ref. [48] for each source. The new values for neutron star properties are summarized in table 4 and displayed in Figure 6. In this analysis, inferred values for z were barely affected. Values of R_∞ , R and M , which now range from 9.4 to 13.2 km, 7.8 to 11 km, and 1.23 to 1.64 M_\odot , respectively, have much smaller variations. The mean value of the inferred radii is about 9.5 km, which is at the lower extremity of values inferred from PRE bursts (§3.1). The source in ω Cen has been confirmed to have an H atmosphere [49]. However, it is possible that one or more of the remaining four QLMXB sources has a He atmosphere rather than an H atmosphere; if so, the inferred radii of those sources having He atmospheres would be increased by approximately 30% as discussed in Ref. [47].

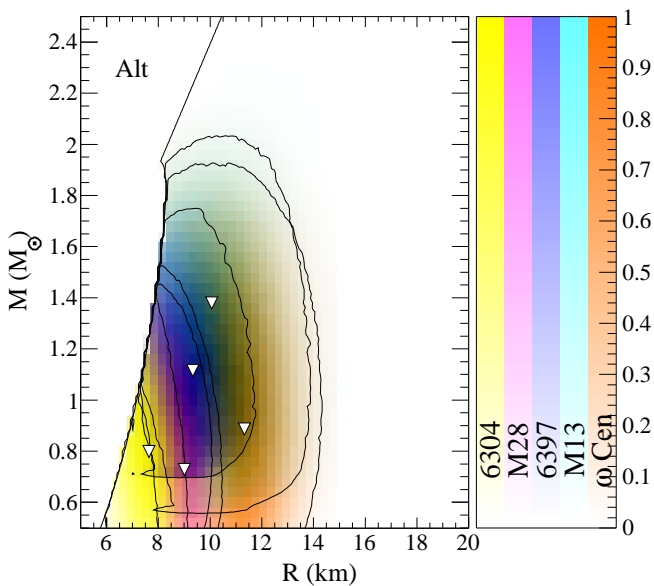


Fig. 6. The same as Figure 5, but M and R probabilities are derived using fixed N_H values from Ref. [48] using the procedure described in the text [47].

4 Bayesian Analysis of Mass and Radius Observations

The basic problem we want to solve is how to compute the M-R curve from a set of neutron star mass and radius observations. We also want the EOS, taking advantage of the well-known bijection between the M-R curves and EOSs provided by the TOV equations. The first critical point is that observations are never perfectly accurate, and thus this problem has an inherently statistical nature: what we really want is the probability distribution of M-R curves and EOSs. The second critical point is that this is a highly underconstrained problem: a curve has an infinite number of degrees of freedom, and we will always have only a finite set of observations. Bayesian statistics is thus already a natural choice, since its application to underconstrained problems is a bit simpler. In an overconstrained least-squares problem, there can be one unique best fit represented by a point in the model space. In the underconstrained system, there is no unique best-fit, but rather an entire subspace inside our model space which consists of “best-fits”. As we will see below, Bayes theorem provides for us a recipe for characterizing that subspace.

The joint probability of event a in event space A and event b in event space B can be denoted $P[A, B]$ (sometimes to be more explicit we write $P[A = a, B = b]$), and can be thought of as a two-dimensional function of a and b . The reader is forewarned that there are a plethora of notations for the same quantity including $P_{A,B}(a, b)$, $P[a, b]$, $P[A \cap B]$, $P[A \text{ and } B]$, and several other options using parentheses instead of or in addition to square brackets. The appropriate units for the joint probability, $[a^{-1}b^{-1}]$,

are clear from the normalization condition

$$1 = \int_A \int_B P[A, B] da db \quad (93)$$

The marginal probability $P[A]$ (with units $[a^{-1}]$) is then given by

$$P[A] = \int_B P[A, B] db \quad (94)$$

and similarly for $P[B]$. The conditional probability is then defined by $P[A|B] \equiv P[A, B]/P[B]$, i.e. the probability of A given B. From this definition, the celebrated “Bayes theorem” can be directly written

$$P[A|B]P[B] = P[B|A]P[A]. \quad (95)$$

In our context, we replace A with the model space \mathcal{M} and B with the “data space” \mathcal{D} (the space of all possible data sets), and

$$P[\mathcal{M}|\mathcal{D}]P[\mathcal{D}] = P[\mathcal{D}|\mathcal{M}]P[\mathcal{M}] \quad (96)$$

where $P[\mathcal{M}|\mathcal{D}]$ is the conditional probability of the model given the data, $P[\mathcal{D}|\mathcal{M}]$ is the conditional probability of the data given the model, and $P[\mathcal{M}]$ and $P[\mathcal{D}]$ are the prior probabilities for the model and the data. By analogy to the definitions above,

$$P[\mathcal{D}] = \int_{\mathcal{M}} P[\mathcal{D}, \mathcal{M}] dm = \int_{\mathcal{M}} P[\mathcal{D}|\mathcal{M}]P[\mathcal{M}] dm \quad (97)$$

(this is sometimes referred to as the “law of total probability”) and thus

$$P[\mathcal{M}|\mathcal{D}] = \frac{P[\mathcal{D}|\mathcal{M}]P[\mathcal{M}]}{\int_{\mathcal{M}} P[\mathcal{D}|\mathcal{M} = m]P[\mathcal{M}] dm} \quad (98)$$

What we want to compute is the conditional probability of all models in our model space, given the data actually observed d inside the space of all possible data sets \mathcal{D} , i.e. $P[\mathcal{M}|\mathcal{D} = d]$. In some cases we only require relative probabilities, i.e. $P[\mathcal{M} = m_1|\mathcal{D} = d]/P[\mathcal{M} = m_2|\mathcal{D} = d]$ for models m_1 and m_2 inside our model space \mathcal{M} , so we do not need to compute the integral in the denominator. The function $P[\mathcal{D}|\mathcal{M}]$ is analogous to the likelihood function familiar from frequentist statistics (as will be described below), and $P[\mathcal{M}]$ is referred to as the prior distribution, reflecting the prior probability of a given model m .

In a typical data set of several one-dimensional data points, the likelihood function is just a multi-dimensional Gaussian, $P[\mathcal{D}|\mathcal{M}] = \exp(-\chi^2/2)$ where

$$\chi^2 = \sum_i \left(\frac{x_{\text{pred},i} - x_{\text{obs},i}}{\sigma_i} \right)^2 \quad (99)$$

Our neutron star data set is inherently two-dimensional, and this is sometimes referred to as a “Type II regression”. A typical frequentist approach is to minimize the distance from the the observed data point (R, M) and the model $M - R$ curve. (This is not entirely unambiguous

because one must still choose the relevant mass and radius scales to measure a distance.) One way to proceed in the Bayesian formalism is to treat the mass of each neutron star as a new model parameter. Our model space, \mathcal{M} , now includes the neutron star masses, M_i in addition to the EOS parameters p_i . In the case that the observations are of the form of two-dimensional Gaussians centered at $(R_{\text{obs},i}, M_{\text{obs},i})$ with width $(\sigma_{R,i}, \sigma_{M,i})$, the conditional probability is

$$P[\mathcal{D}|\mathcal{M}] = \prod_{i=1}^{N_O} (2\pi\sigma_{M,i}\sigma_{R,i})^{-1} \times \exp \left[-\frac{1}{2} \left(\frac{M_i - M_{\text{obs},i}}{\sigma_{M,i}} \right)^2 - \frac{1}{2} \left(\frac{R_i(M_i, \{p_j\}) - R_{\text{obs},i}}{\sigma_{R,i}} \right)^2 \right] \quad (100)$$

for N_O neutron star observations. It is the evaluation of the function $R_i(M_i, p_j)$ here which requires a solution of the TOV equations for each point in the model space. In general, the observations are not two-dimensional Gaussians, and the conditional probability for each observation is a general distribution $\mathcal{D}_i(R_i, M_i)$ normalized so that

$$1 = \int dR_i dM_i \mathcal{D}_i(R_i, M_i). \quad (101)$$

The full prior probability, $P[\mathcal{M}]$, in this context is now an $(N_P + N_O)$ -dimensional function reflecting the prior probability given a set of N_P EOS parameters and N_O neutron star masses. It is reasonable to assume that the prior can be factorized into separate prior distributions for the EOS and the masses. A simple uniform prior distribution for the EOS parameters is not unreasonable. A physical interpretation for the prior on the neutron star masses is that it is equal to the neutron star initial mass function, which we will vary below.

Bayes theorem itself is a result which can be obtained from basic axioms of probability theory. The frequentist and Bayesian approaches diverge in how the theorem ought to be applied. The standard Bayesian approach is to compute the desired results by integrating (marginalizing) over the parameters not currently being considered. Explicitly, for the posterior probability distribution of one of the EOS parameters, p_i , one computes the integral

$$P[p_i] = \int P[\mathcal{D}|\mathcal{M}]P[\mathcal{M}]dp_1 dp_2 \dots dp_{i-1} dp_{i+1} \dots dp_{N_P} dM_1 \dots dM_{N_O} \quad (102)$$

After normalizing the posterior distribution, one can compute the ‘‘Bayesian confidence region’’. When the posterior is sufficiently unimodal, the 68% confidence region is the range (p_{iL}, p_{iR}) surrounding the maximum value of $P[p_i]$ for which

$$0.68 = \int_{p_{iL}}^{p_{iR}} P[p_i] dp_i \quad (103)$$

and $P[p_{iL}] = P[p_{iR}]$. For a multimodal distribution, the 68% confidence region is the region $\mathcal{S}_i(\eta)$, defined as the union of all intervals over p_i for which $P[p_i] > \eta$, which is obtained by solving $\int_{\mathcal{S}_i(\eta)} P[p_i] dp_i = 0.68$ for η .

Alternatively, one can write $P[p_i]$ using a δ -function, and a helpful simplification comes from the fact that we can write almost all the quantities of interest using the same kernel, $P[\mathcal{D}|\mathcal{M}]P[\mathcal{M}]$. The expressions

$$\begin{aligned} P[p_i = \hat{p}_i] &= \int \delta(p_i - \hat{p}_i) \times \\ &\quad P[\mathcal{D}|\mathcal{M}]P[\mathcal{M}]d\{p\}d\{M\} \\ P[R(M) = \hat{R}, M = \hat{M}] &= \int \delta[R(\hat{M}) - \hat{R}] \times \\ &\quad P[\mathcal{D}|\mathcal{M}]P[\mathcal{M}]d\{p\}d\{M\} \\ P[\epsilon = \hat{\epsilon}, P(\epsilon) = \hat{P}] &= \int \delta[P(\hat{\epsilon}) - \hat{P}] \times \\ &\quad P[\mathcal{D}|\mathcal{M}]P[\mathcal{M}]d\{p\}d\{M\} \end{aligned} \quad (104)$$

give the posterior distributions for the parameters, the probability distribution for the radius given a fixed mass (the M-R curve), and the probability distribution for the pressure given a fixed energy density (the EOS), respectively. Unless we are computing the Bayes factor (defined below), we only need to determine these integrals up to a scale factor and one can replace the δ -functions by pairs of step-functions, i.e.

$$\delta(P - \hat{P}) \rightarrow \theta[P - (\hat{P} - \Delta P)]\theta[(\hat{P} + \Delta P) - P] \quad (105)$$

One can perform a single Markov chain Monte Carlo simulation of the integration kernel $P[\mathcal{D}|\mathcal{M}]P[\mathcal{M}]$, and construct a histograms to select only those points in the chain which satisfy the conditions given by the step-functions in the various integrals.

4.1 Simplified Models Without Equations of State

A simple model, suggested by Ref. [46] partly based on results from Ref. [50], is that all neutron stars have the same radius. This model is beneficial because it contains no assumptions about the nature of the compact objects being observed. In this case, the model space has only one parameter, and the only remaining integrals are those over the individual neutron star masses. We also assume uniform prior distributions for all of the neutron star masses corresponding to flat neutron star initial mass functions. In the case that the observations are two-dimensional Gaussians, the integrals over the masses are trivial Gaussian integrals and Equation (102) can be written

$$P(R) = \prod_{i=1}^{N_O} (2\pi)^{-1/2} \sigma_{R,i}^{-1} \exp \left[-\frac{1}{2} \left(\frac{R - R_{\text{obs},i}}{\sigma_{R,i}} \right)^2 \right]. \quad (106)$$

This is proportional to the frequentist likelihood function for N_O neutron star radius measurements and the peak

of this distribution is exactly the radius which minimizes the corresponding χ^2 .

We use this simple "common radius" model to analyze both the PRE observations (with $z_{\text{ph}} = 0$ as in Fig. 3) and the QLMXB observations. One can enforce causality with the additional restriction $R_i < 2.94 GM_i$ for each object. It is clear from Fig. 5 that there are very few radii which intersect the regions for the neutron star in ω Cen and the other four neutron stars. If all neutron stars indeed have the same radius, the probability of actually observing the data given in Fig. 5 would be extremely small. After the adjustment for the hydrogen column densities described in section 3.2 above and obtaining the results in Fig. 6, there are several vertical lines which go through all the data sets, and the Bayesian 95% confidence interval for the neutron star radius is 10.8 ± 1.2 km. Our result is not significantly different from the range of radii earlier predicted in Ref. [50], in part because the average PRE data with $z = 0$ discussed in §3.1 also has $\bar{R} = 10.8$ km and partly because the QLMXB data was analyzed with similar assumptions regarding the hydrogen column density in both cases. Our predicted radius is larger than in G13 for this common radius model by about 1.5 km to 2.8 km, depending on whether N_H values are frozen at their "best-fit" values or not. This difference cannot be attributed to different assumptions for N_H , because the average radius found by Ref. [47] are actually 1.6 km smaller than found by Ref. [46]. Partly, the difference is due to the unequal weighting assigned to individual sources in Ref. [46] on the basis of the relative quality of the observational data: the source with the smallest individual radius, in NGC 6397, has 35% of the statistical weight and the source with the largest individual radius, in ω Cen, has 7.8% of the statistical weight [46]. This unequal weighting only partially explains G13's small common radius. With unequal weighting, their average radius is reduced to 9.8 km, still larger than their common radius.

There is a straightforward explanation why the common radius found by Ref. [46] is as much as 1.7 km smaller than their average value [47]. The key is that values of R_∞ found by Ref. [46] in their joint analysis of QLMXBs are nearly the same as those found in their independent determinations. Because R_∞ is determined with greater accuracy than z , the joint analysis can find a common radius by shifting the value of z for each source. We can thus estimate the common radius R by minimizing the function

$$\chi^2 = \prod_i \left\{ \exp \left(-w_i \left[\frac{z(R, R_{\infty,i}) - z(R_i, R_{\infty,i})}{\Delta_i} \right]^2 \right) \right\} \quad (107)$$

with respect to R . R_i , $R_{\infty,i}$, w_i and Δ_i are the radius, R_∞ , weight and z uncertainty, respectively, associated with source i . Since $z(R, R_\infty) + 1 = R_\infty/R$, minimization leads to

$$R = \sum_i \frac{w_i R_{\infty,i}^2}{\Delta_i^2} \bigg/ \sum_i \frac{w_i R_{\infty,i}^2}{R_i \Delta_i^2} \simeq 8.1 \text{ km}, \quad (108)$$

nearly the value (8 ± 1) km Ref. [46] found when N_H values were assumed frozen.

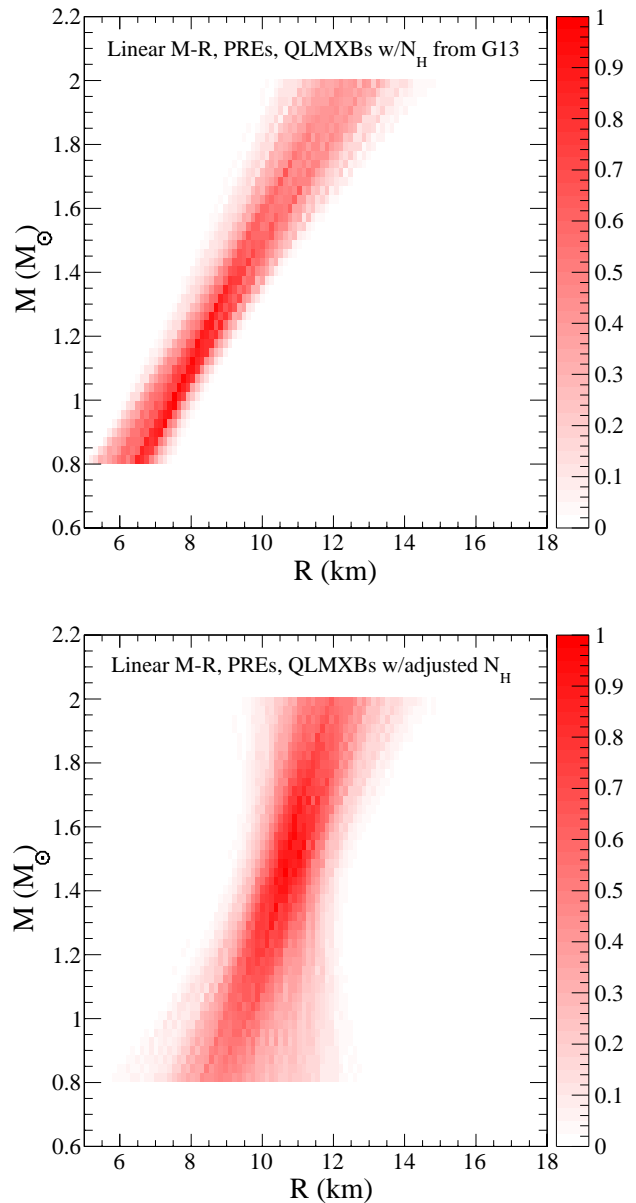


Fig. 7. $M - R$ curves obtained from the PRE and QLMXB data under the assumption that the $M - R$ curve is a line with constant slope. The top panel gives results assuming that for the QLMXBs, N_H is given by the values in G13. The bottom panel uses the adjusted values of N_H from Ref. [48]. The PRE (R, M) distributions are the same for both panels.

An alternative model with two parameters assumes that the $M - R$ curve is a line with arbitrary slope. The top panel in Figure 7 gives the results assuming the hydrogen column densities from Ref. [46] and the bottom panel gives the results assuming the adjusted hydrogen column densities from Ref. [48] and allowing for the presence of helium atmospheres. The PRE sources are treated the same in both panels, under the assumption that $z_{\text{ph}} = 0$ at touchdown. The results are cut off for masses above $\hat{M} = 2M_\odot$ and we use $0.8M_\odot$ as a lower limit. Both sets of $M - R$

line distributions, independent of the assumptions about the hydrogen column densities, show a clear preference for very small radii for low-mass stars. In the context of current models of neutron stars with crusts based on modern nucleon-nucleon interactions, such small radii are very difficult without very small values of L and strong phase transitions just above the nuclear saturation density.

Note that by using a different prior distribution for two model parameters (slope and y-intercept), this alternative model would give exactly the same results as the previous model. The previous “vertical line” model can be obtained by assuming a delta-function prior distribution which ensures the line is vertical. Similarly, given a fixed data set, any model “B” for the distribution of $M - R$ curves is equivalent to any other model “A”, if one modifies the prior distribution for model B so that

$$P[\mathcal{M}_B] = P[\mathcal{D}|\mathcal{M}_A]P[\mathcal{M}_A]/P[\mathcal{D}|\mathcal{M}_B]. \quad (109)$$

This shows that choosing an alternate EOS parameterization is equivalent to choosing a different prior distribution for the original EOS parameters.

Finally, we consider more generic $M - R$ curves, made up of four line segments with masses between 1 and $2M_\odot$ with a total of 8 parameters. The results are given in Figs. 8 and 9. The top panel of Fig. 8 and the top panel of Fig. 9 show different assumptions for the hydrogen column densities and atmospheric composition as before. The bottom panel of Fig. 8 shows results with the values of N_H from Ref. [48] for the QLMXBs and with $z_{\text{ph}} = z$ for the PREs. Small radii are still preferred for low mass neutron stars. This will be the most significant difference between models with no assumptions about low-density matter and the results given below.

It is important to note here that Figs. 7, 8, and the top panel of Fig. 9 represent a set of one-dimensional histograms: one histogram for each fixed mass \hat{M} as in Equation (104), each of them separately normalized, and then plotted together. The distribution of radii for a $1M_\odot$ neutron star has a smaller density (lighter color) than the distribution of the radii for a $1.5M_\odot$ because the distribution is broader, i.e. the radius of a $1M_\odot$ neutron star is less well-constrained. This does not mean that $1M_\odot$ neutron stars are less probable than $1.5M_\odot$ neutron stars. Also, while it is tempting to see the general $M - R$ curve in the top panel of Fig. 9 as nearly linear, this does not mean that the radius of a low-mass and the radius of a high-mass neutron star are necessarily correlated (in this model). Several $M - R$ curves from the same simulation in the top panel of Fig. 9 are given in bottom panel of Fig. 9. These curves can contain kinks at moderate masses which effectively decouple the low- and high-mass properties of the typical $M - R$ curve. Note also that many of these $M - R$ curves are incompatible with the TOV equations and physical EOSs.

4.2 Models With Equations of State

We now employ the model of Ref. [37], using a neutron star crust, a phenomenological EOS near the saturation

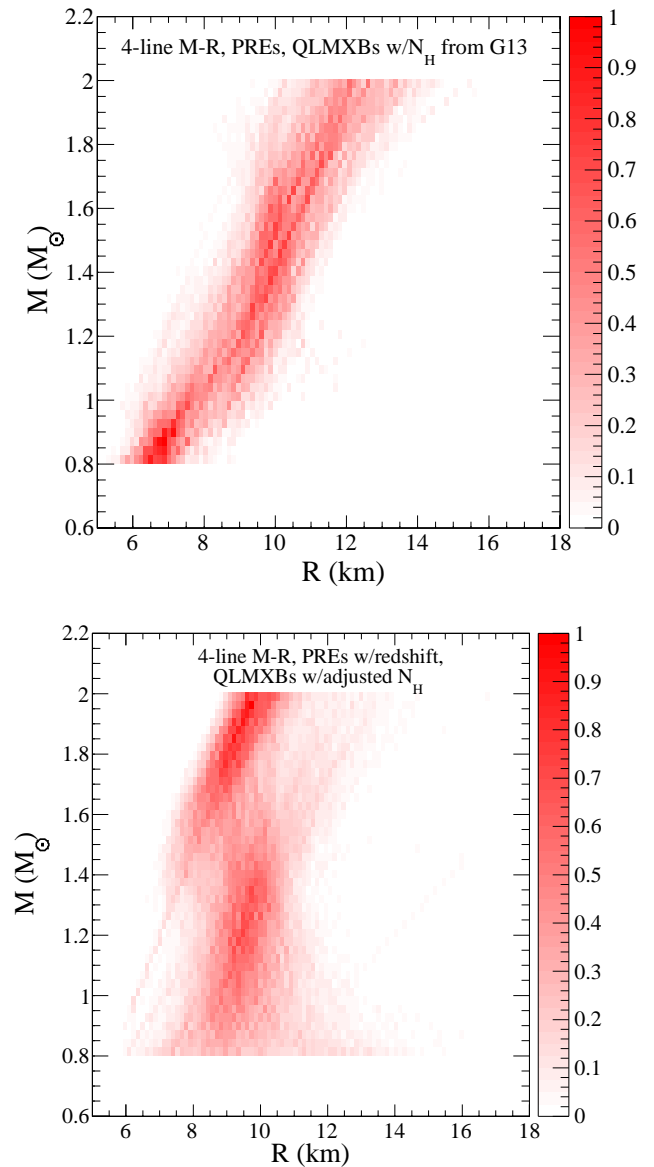


Fig. 8. $M - R$ curves obtained from the PRE and QLMXB data for a generic $M - R$ curve made from four line segments. The top panel assumes that $z_{\text{ph}} = 0$ for the PRE sources and the G13 values for N_H for the QLMXBs. The bottom panel assumes that the photosphere is redshifted for the PRE sources and uses the values of N_H from Ref. [48] for the QLMXBs.

density, and the implicit assumption that the TOV equations relate the EOS to M and R . At higher densities, we use two polytropes. (This is also referred to as “Model A” in Ref. [50].) For now, we keep the same uniform initial mass function for each neutron star in the sample. In addition to causality, we now ensure that the maximum mass is above 2 solar masses. We use the alternative hydrogen column densities from Ref. [48] and allow for both hydrogen and helium atmospheres (except for the source in ω Cen) for the QLMXBs, and take $z_{\text{ph}} = 0$ for the PRE sources. The predicted $M - R$ distribution for the full set

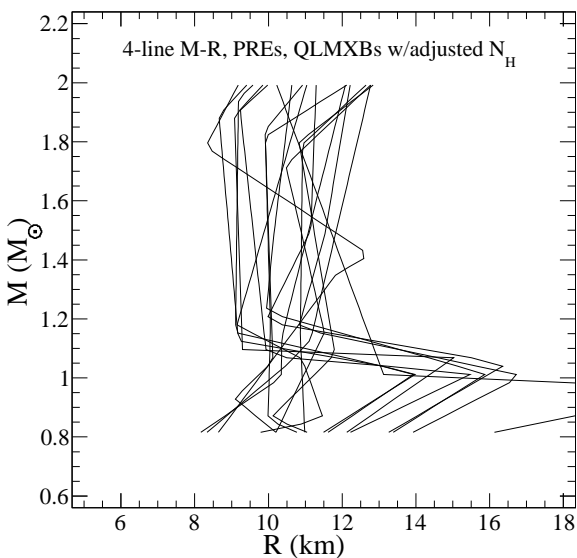
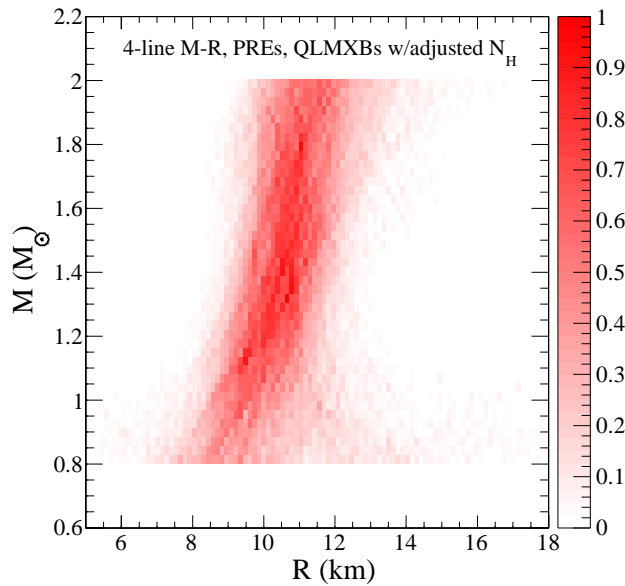


Fig. 9. The top panel is the same as in Figure 8 except that the values for N_H for the QLMXBs are taken from Ref. [48]. The bottom panel gives a small sampling of $M-R$ curves used to construct the distributions in the top panel.

of 5 PRE and 5 QLMXB sources is shown in Figure 10 and observed to be relatively vertical. This is a natural consequence of (i) causality, (ii) the requirement of generating a 2 solar mass neutron star, (iii) the existence of a neutron star hadronic crust, and (iv) the observation of neutron stars with inferred small values of R_∞ . The $M-R$ curve also predicts larger radii for low-mass neutron stars. The range of radii for a $1.4M_\odot$ neutron star, 11.3–12.1 km (68% confidence) is also slightly larger than that suggested by the same model (model A) in Ref. [50], a consequence of the larger radii implied by the possibility of helium atmospheres in four of the QLMXB sources.

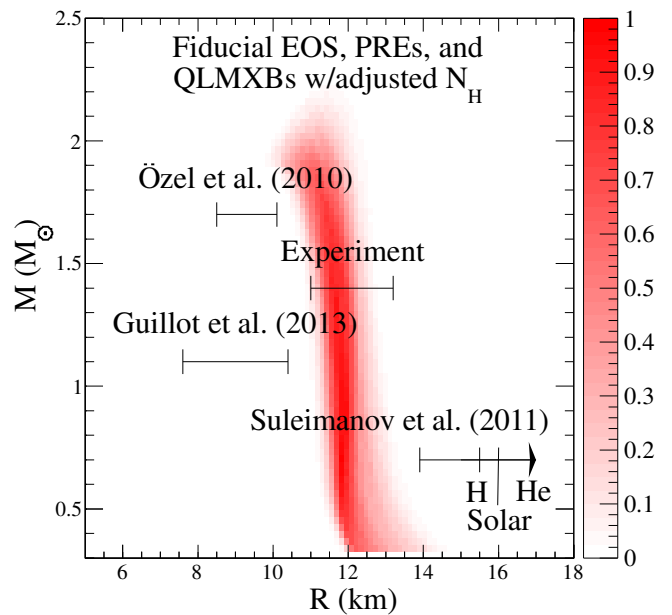


Fig. 10. Probability distributions for M and R for the five PRE burst sources, assuming $z_{\text{ph}} = 0$, and five QLMXB sources, assuming adjusted values of N_H from Ref. [48] and the possibility of either H or He atmospheres for four of the sources. The EOS is parametrized with two polytropes at high density. The radius ranges implied by the analyses of Özel et al. (95% confidence weighted average [44,42,43]), Guillot et al. (joint analysis assuming a fixed radius for all masses [46]), Suleimanov et al. (90% confidence intervals for pure H, solar with $Z = 0.02$, and pure He atmospheres [51]), and nuclear experiments (90% confidence interval for $1.4M_\odot$ stars, §2.4) are also shown (with arbitrary vertical locations).

The 90% confidence range for the radius of $1.4M_\odot$ stars is tabulated in table 5, and the corresponding EOS is given in Figure 11, along with the pressure ranges at an energy density of 600 MeV/fm^3 from Refs. [50] and [35].

Fig. 12 gives the posterior (R, M) distribution for just one of the 10 neutron stars, the QLMXB in M13. (This posterior distribution is a true two-dimensional histogram, unlike that in Fig. 10.) Note that this posterior distribution for the neutron star in M13 is much more strongly-peaked than the input (R, M) distribution for M13 which was used in the simulation (which is similar to that shown in Figure 6 assuming an H atmosphere). The posterior (R, M) distribution lies along the predicted $M-R$ curve (as it must) and implies that this neutron star is likely to have $M < 1.8M_\odot$.

It is natural to inquire how sensitive our results are to the nature of the astronomical sources utilized. Table 5 shows that the 90% confidence intervals for the radii of $1.4M_\odot$ stars is increased by 0.3–0.4 km if only PRE burst sources are considered, while the radii are increased by 0.1–0.2 km if only QLMXB sources are included. These small differentials imply that our results are not very sensitive to the type of source included, and that the constraints of maximum mass, causality, a hadronic crust

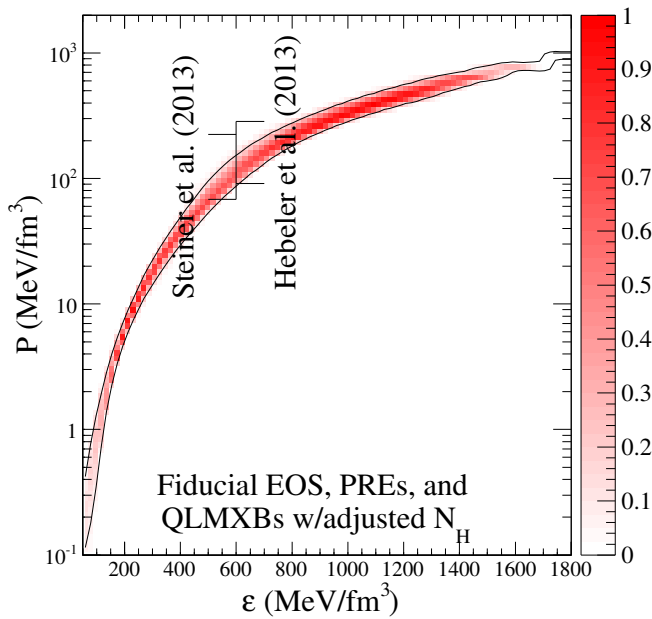


Fig. 11. Probability distributions for pressure and energy density from the Bayesian analysis of 5 PRE and 5 QLMXB sources under the same conditions as in Fig. 10. Also shown are two representative ranges for the pressure from Refs. [50] and [35].

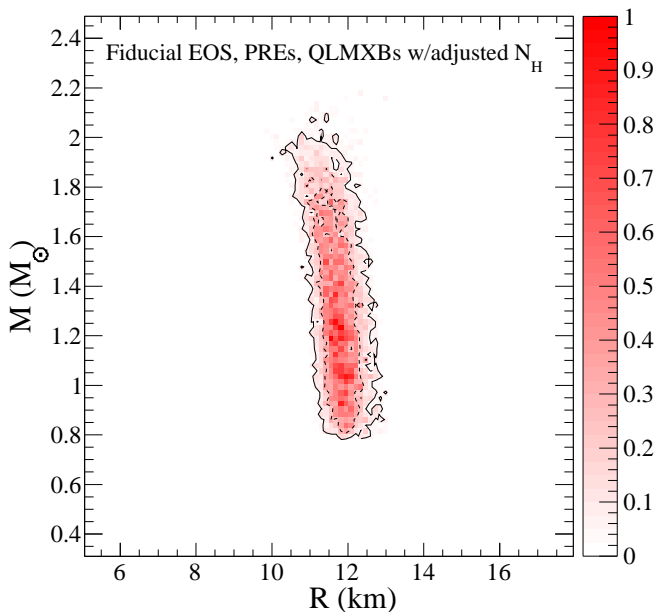


Fig. 12. Probability distributions for M and R of the neutron star in M13 with the same assumptions as given for Figure 10.

EOS and the TOV equation are powerful. The lower limit on the radius from QLMXB sources in the last row is 11.2 km, and adding the PRE sources (which have significant probability at low radius) implies a only a slightly smaller lower limit of 11.1 km. In short, limits to L are not much affected by the type of source included in our analyses.

The neutron star observations constrain the nuclear symmetry energy, as expected from the correlation described in Eq. 8 above. The corresponding constraint, from our preferred model, on L is between 37.0 and 55.3 MeV, to 68% confidence. This range is similar to that found for Model A in Ref. [50] except the lower range for L has been decreased because of the very small radii of the neutron stars in globular clusters NGC 6304 and M28. Using a different EOS parameterization which allows for stronger phase transitions (e.g., model C in Ref. [50]) increases the upper 68% confidence limit on L to about 65 MeV. This happens because a phase transition partially decouples the low- and high-density behavior of the EOS, allowing small radii even if L is relatively large.

4.3 Alternative Mass Distributions

One can assess the effects of a different neutron star initial mass function by modifying the prior distribution for the neutron star masses. We assume the same mass distribution as in that Ref. [36], which is obtained summing the mass probability distributions for each star, weighting each of them equally. The individual probability distributions are assumed to be Gaussians centered on the tabulated masses, with their 1σ error widths. The top panel of Fig. 13 shows this prior mass distribution and the bottom panel shows the resulting posterior (R, M) distribution for the neutron star in M13. The sharp peaks in the initial mass function naturally lead to a stronger mass and radius constraint for this neutron star.

4.4 Bayes Factors

To compare two models, \mathcal{M}_1 and \mathcal{M}_2 , one uses the Bayes factor

$$B_{12} = \frac{\int_{\mathcal{M}_1} P[\mathcal{D}|\mathcal{M}_1 = m_1]P[\mathcal{M}_1 = m_1] dm_1}{\int_{\mathcal{M}_2} P[\mathcal{D}|\mathcal{M}_2 = m_2]P[\mathcal{M}_2 = m_2] dm_2} \quad (110)$$

If $B_{12} > 1$, then model 1 is preferred, and if $B_{12} < 1$, then model 2 is preferred. A typical phrasing is that $B_{12} > 3$ implies the evidence for model 1 is substantial, $B_{12} > 10$ implies the evidence is strong, $B_{12} > 30$ implies the evidence is very strong, $B_{12} > 100$ implies the evidence is decisive. In contrast to the integrals in Equation (104), the normalization of the integrals in the Bayes factor is important. In addition, the same Markov chain cannot be trivially used to compute the Bayes factor, and so it typically requires separate Monte Carlo integrations. Because the integrands in Equations (104) and (110) demand a solution of the TOV equations at every point, they are computationally expensive. However, we have found that

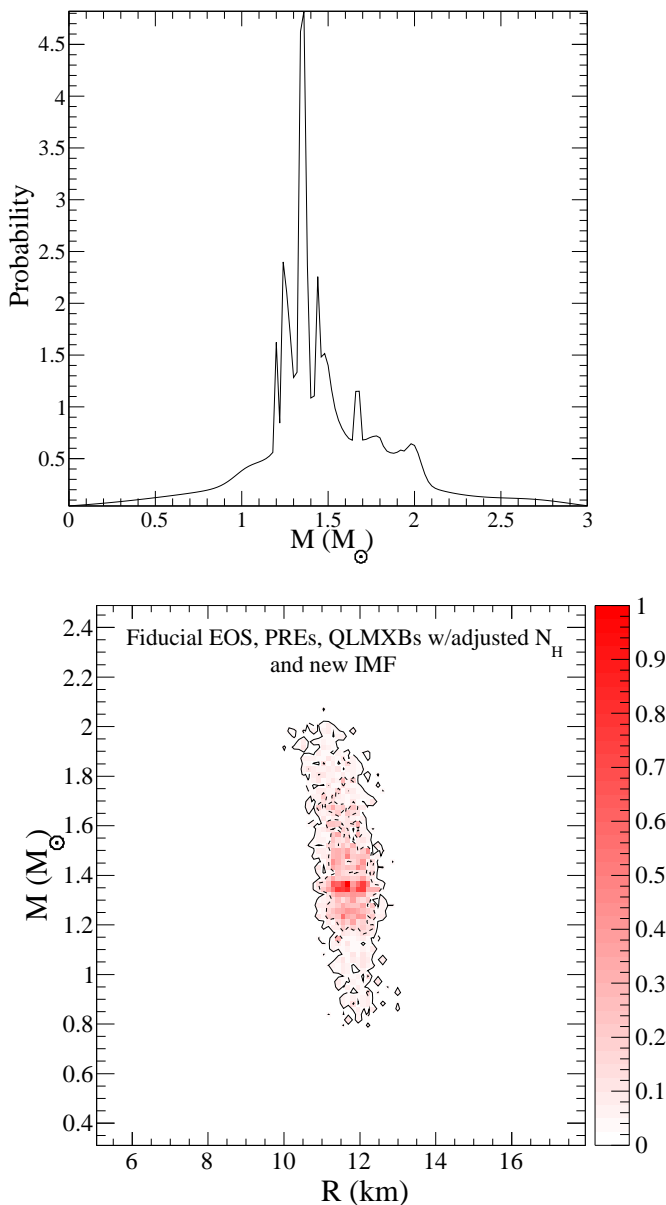


Fig. 13. The top panel shows the mass distribution inferred from the mass data in Ref. [36] and the bottom panel shows the posterior mass and radius distribution of the neutron star in M13 having used the PRE and QLMXB data as in Fig. 10 but assuming the neutron star mass function is as given in the top panel.

the Markov chains created to compute the integrals in Equation (104) can be re-used with a simple interpolation scheme to avoid having to solve the TOV equations again for the integrations in Equation (110).

Note that, in this Bayesian formalism, the actual number of parameters plays very little role. This is in contrast to the frequentist approach where one must divide χ^2 by the number of “degrees of freedom” in order to determine the goodness-of-fit. Nevertheless, the Bayes factor can act as an Occam’s razor, disfavoring models which have “ex-

tra” parameters. Thus it is often not necessary to choose models with the minimum number of parameters, as the Bayes factor comparison will select the preferred model automatically.

The Bayes factor provides a quantitative statistical method for determining whether or not the Eddington flux at touchdown ought to be redshifted in PRE X-ray bursts. When Monte Carlo trial points for $z_{\text{ph}} = z$ are rejected due to the fact that they lead to unphysical masses and radii, they cannot contribute to the integral in Equation (110). Ref. [37] found that, in each case, at least 90% of the trials are rejected for a typical PRE X-ray burst source. For one neutron star, this would lead to a Bayes factor of 10 at least in support of $z_{\text{ph}} = 0$. Because of the product appearing in Equation (100), one must count a factor of at least 10 for each neutron star, leading to overwhelming support of the model that the photosphere is not fully redshifted at touchdown.

The Bayes factor can also be used to test the alternative values for the hydrogen column densities described in section 3.2. Table 5, adapted from LS13, contains the computed 90% confidence limits for the radius of $1.4M_{\odot}$ stars for all QLMXBs under different scenarios. “Base” assumes N_H values from G13 and H atmospheres for all sources, “Alt” uses the alternative values of N_H from Ref. [48] and H atmospheres for all sources, “H+He” uses N_H values from G13 but allows for either He or H atmospheres for all sources except the one in ω Cen, and “Alt/H+He” uses N_H values from Ref. [48] and allows for either He or H atmospheres. The integral for computing the Bayes factor, sometimes called the “evidence”, is given in the last column for the QLMXB only cases. The Bayes factor for comparing the alternative hydrogen column densities to those given in G13 is very large $\sim 10^6$ (from the ratio of the evidence in the first two rows of the table), showing the alternative model is strongly preferred. Almost as preferred is the model in which G13 hydrogen column densities are used, but the possibility of either H or He atmospheres for four of the sources is entertained. Finally, the combination of the alternative column densities from Ref. [48] plus the possibility of either H or He atmospheres is greatly preferred to the other scenarios.

5 Discussion

A plethora of nuclear experimental data indicates that the symmetry energy parameters S_v and L are constrained to a greater degree than just a few years ago. Although these constraints have varying degrees of model dependence that need to be further explored, they are well-supported by studies of pure neutron matter, which can determine these parameters assuming that higher-than-quadratic terms in the symmetry energy expansion in neutron excess are ignored. It is expected that future theoretical studies of neutron matter with small proton concentrations will allow the validity of the quadratic expansion to be ascertained. From studies of solutions to the hydrostatic structure equations in general relativity [1], these

Table 5. 90% confidence ranges for radii of $1.4M_{\odot}$ stars and integrals I for computing the Bayes factor for various models (see the text).

Model	$R_{1.4}$ 90% confidence range	I
Alt/H+He QLMXB; $z = 0$ PRE	11.13 – 12.33	
$z = 0$ PRE only	11.56 – 12.64	
Base, QLMXB only	11.01 – 11.94	$(1.77 \pm 0.09) \times 10^{-8}$
Alt, QLMXB only	10.62 – 11.50	$(4.65 \pm 0.48) \times 10^{-3}$
H+He, QLMXB only	11.29 – 12.83	$(4.50 \pm 0.21) \times 10^{-3}$
Alt/H+He, QLMXB only	11.24 – 12.59	$(2.14 \pm 0.19) \times 10^{+2}$

symmetry energy restrictions and the quadratic approximation allow the radii of neutron stars to be determined to about 10% accuracy [2]. For the experimental constraints studied here, the deduced radius of $1.4M_{\odot}$ neutron stars is $R_{1.4} = 12.1 \pm 1.1$ km. Neutron matter studies suggest slightly smaller values by about 0.2 km.

In comparison, the astrophysical determination of individual neutron star radii have much less precision. Nevertheless, Bayesian studies (cf., [37,50]) of the ensemble of individual sources for which both mass and radius information is available, imply typical radii (i.e., for $1.2 - 1.8M_{\odot}$ stars) in the range 11.2 – 12.8 km. There is emerging an important interplay between the nuclear physics and the astronomical observations: *we find a concordance between the observations and the nuclear experiments*. With almost any reasonable assumptions regarding the nature of the EOS at high densities and the parameters of models for shorter PRE X-ray bursts and QLMXBs, the powerful constraints of causality, observations of $2M_{\odot}$ neutron stars, and the existence of a nuclear neutron star crust, lead to $M - R$ curves which are nearly vertical and radii for moderate-mass neutron stars that are compatible with nuclear data and theoretical studies of neutron matter.

Thus, neutron star mass and radius observations are clearly beginning to make quantitative constraints on both the EOS and the parameter L which describes the density dependence of the symmetry energy. Two major classes of neutron star observations have provided important constraints: PRE X-ray bursts and the surface emission of QLMXBs. In both of these classes of neutron star observations, the theoretical models which interpret X-ray photons and produce the inferred neutron star mass and radius are an important source of uncertainty.

PRE X-ray bursts are interpreted as resulting from the vertical motion of the photosphere. Assumptions about the position of the photosphere at touchdown can change radius estimates by about 2 km. If the photosphere of PRE X-ray burst neutron stars is redshifted at touchdown, we find that the observed fluxes and normalizations tend to be inconsistent with the model, judging from the small number of Monte Carlo trials over the observed uncertainty ranges of touchdown fluxes, distances, and normalizations that result. In addition, the 95% confidence radius range from Ref. [42,43,44], which comes from PRE sources alone and assumes the photosphere at touchdown is at the stellar surface, i.e., $z_{\text{ph}} = z$, is also incompatible with nuclear experiment, as seen in Figure 10. However, these are not the only difficulties surrounding the interpre-

tation of PRE X-ray bursts, and color correction factors and composition are also important uncertain parameters. For example, Suleimanov et al. have argued [51] that the short PRE bursts studied by Ozel et al. and in this contribution might have significant disk absorption and f_c evolution during the burst that would dramatically increase the inferred radii. Ref. [51] instead studied longer PRE bursts and found radii in excess of 13.9 km to 90% confidence (Figure 10), assuming stellar masses less than $2.3M_{\odot}$. Importantly, both the ranges suggested by Ozel et al. and Suleimanov et al. are inconsistent with nuclear systematics.

In the case of QLMXBs, there is no photospheric dynamics to complicate the interpretation of the neutron star atmosphere, but the composition of the atmosphere and the magnitude of X-ray absorption between us and the source are both major uncertainties. Differences of assumed X-ray absorption magnitudes result in both larger and smaller radii. If the hydrogen column densities are assumed to be those obtained from self-consistent fitting of X-ray spectra [46], in some cases the observed neutron stars are (i) too small to satisfy causality limits, and (ii) too large to be consistent with the available nuclear data and any reasonable neutron star model. On the basis of our Bayesian model, however, we conclude that, on average, N_H values from Ref. [48] are statistically favored in comparison to those obtained from self-consistently fitting [46] the X-ray spectra. The alternative N_H values also lead to a more uniform distribution of masses and radii among the sources. The radius range deduced by G13 in their joint study in which it is assumed that all neutron stars have the same radius is inconsistent with both our results from the joint study of PRE bursts and QLMXBs and with inferences from nuclear experiments to 90% confidence.

The large degree of model-dependence in interpreting astronomical observations suggests more sophisticated modeling is in order. It will be necessary to model PRE bursts using hydrodynamical radiation transport simulations to fit the overall light-curve behavior to fully resolve the discrepancies and to provide reliable M and R estimates. Similarly, for the QLMXBs, there is a clear necessity of obtaining further observations for fixing the interstellar X-ray absorption for QLMXBs. Moreover, there is evidence that models of QLMXBs allowing for the possibility of He as well as H atmospheres are favored, a question which further observations may also be able to decide.

Acknowledgements

J. M. L. is supported by the U.S. DOE grant DE-AC02-87ER40317 and A. W. S. is supported by U.S. DOE Grant DE-FG02-00ER41132.

References

1. J. M. Lattimer and M. Prakash, *Astrophys. J.* **550**, 426 (2001).
2. J. M. Lattimer and Y. Lim, *Astrophys. J.* **771**, 51 (2013).
3. P. B. Demorest, T. Pennucci, S. M. Ransom, M. S. E. Roberts, and J. W. T. Hessels, *Nature* **467**, 1081 (2010).
4. J. Antoniadis, P. C. C. Freire, N. Wex, T. M. Tauris, R. S. Lynch, *et al.*, *Science* **340**, 448 (2013).
5. G. Audi, A. H. Wapstra, and C. Thibault, *Nucl. Phys. A* **729**, 337 (2003).
6. W. D. Myers and W. J. Swiatecki, *Ann. Phys.* **55**, 395 (1969).
7. E. Lipparini and S. Stringari, *Phys. Rep.* **175**, 103 (1989).
8. W. D. Myers and W. J. Swiatecki, *Nucl. Phys. A* **81**, 1 (1966).
9. A. W. Steiner, M. Prakash, J. M. Lattimer, and P. J. Ellis, *Phys. Rep.* **411**, 325 (2005).
10. P. Danielewicz, *Nuc. Phys. A* **727**, 233 (2003).
11. M. Kortelainen, T. Lesinski, J. Moré, W. Nazarewicz, J. Sarich, *et al.*, *Phys. Rev. C* **82**, 024313 (2010).
12. W. D. Myers and W. J. Swiatecki, *Ann. Phys.* **204**, 401 (1990).
13. P. Möller, W. D. Myers, H. Sagawa, and S. Yoshida, *Phys. Rev. Lett.* **108**, 052501 (2012).
14. S. Gandolfi, J. Carlson, and S. Reddy, *Phys. Rev. C* **85**, 032801 (2012).
15. K. Hebeler, J. M. Lattimer, C. J. Pethick, and A. Schwenk, *Phys. Rev. Lett.* **105**, 161102 (2010).
16. L.-W. Chen, C. M. Ko, B.-A. Li, and J. Xu, *Phys. Rev. C* **82**, 024321 (2010).
17. L. Ray, *Phys. Rev. C* **19**, 1855 (1979).
18. A. Krasznahorkay, J. A. Balanda, J. A. Bordewijk, M. N. Brandenburg, *et al.*, *Nucl. Phys. A* **567**, 521 (1994).
19. A. Krasznahorkay, P. Fujiwara, P. van Aarlo, H. Akimune, I. Daito, *et al.*, *Phys. Rev. Lett.* **82**, 3216 (1999).
20. A. Trzeinska, P. Jastrzebski, F. J. Hartmann, R. Schmidt, T. von Egidy, and B. Klos, *Phys. Rev. Lett.* **87**, 082501 (2001).
21. A. Klimkiewicz, N. Paar, P. Adrich, M. Fallot, K. Boretzky, *et al.*, *Phys. Rev. C* **76**, 051603(R) (2007).
22. S. Terashima, H. Sakaguchi, H. Takeda, T. Ishikawa, M. Itoh, *et al.*, *Phys. Rev. C* **77**, 024317 (2008).
23. A. Tamii, I. Poltoratska, P. von Neumann-Cosel, Y. Fujita, T. Adachi, *et al.*, *Phys.Rev.Lett.* **107**, 062502 (2011).
24. X. Roca-Maza, M. Brenna, G. Coló, M. Centelles, X. Viñas, *et al.*, *Phys. Rev. C* **88**, 024316 (2013).
25. P.-G. Reinhard and W. Nazarewicz, *Phys. Rev. C* **81**, 051303 (2010).
26. L. Trippa, G. Coló, and E. Vigezzi, *Phys. Rev. C* **77**, 061304 (2008).
27. M. B. Tsang, Y. Zhang, P. Danielewicz, M. Famiano, Z. Li, W. G. Lynch, and A. W. Steiner, *Phys. Rev. Lett.* **102**, 122701 (2009).
28. P. Danielewicz and J. Lee, *Nucl. Phys. A* **922**, 1 (2014).
29. D. V. Shetty, S. J. Yennello, and G. A. Souliotis, *Phys. Rev. C* **76**, 024606 (2007).
30. E. Friedman, *Nucl. Phys. A* **896**, 46 (2012).
31. B. C. Clark, L. Kerr, and S. Hama, *Phys. Rev. C* **67**, 054605 (2003).
32. J. Zenhiro *et al.*, *Phys. Rev. C* **82**, 044611 (2010).
33. V. E. Starodubsky and N. M. Hintz, *Phys. Rev. C* **49**, 2118 (1994).
34. A. W. Steiner and S. Gandolfi, *Phys. Rev. Lett.* **108**, 081102 (2012).
35. K. Hebeler, J. M. Lattimer, C. J. Pethick, and A. Schwenk, *Astrophys. J.* **773**, 11 (2013).
36. J. M. Lattimer, *Annu. Rev. Nucl. Part. Sci.* **62**, 485 (2012).
37. A. W. Steiner, J. M. Lattimer, and E. F. Brown, *Astrophys. J.* **722**, 33 (2010).
38. F. Özel, *Nature* **441**, 1115 (2006).
39. F. Özel, T. Güver, and D. Psaltis, *Astrophys. J.* **693**, 1775 (2009).
40. T. Güver, F. Özel, A. Cabrera-Lavers, and P. Wroblewski, *Astrophys. J.* **712**, 946 (2010).
41. T. Güver, P. Wroblewski, L. Camarota, and F. Özel, *Astrophys. J.* **719**, 1807 (2010).
42. F. Özel, A. Gould, and T. Güver, *Astrophys. J.* **748**, 5 (2012).
43. T. Güver and F. Özel, *Astrophys. J.* **765**, 1 (2013).
44. F. Özel, G. Baym, and T. Güver, *Phys. Rev. D* **82**, 101301 (2010).
45. J. Wilms, A. Allen, and R. McCray, *Astrophys. J.* **542**, 914 (2000).
46. S. Guillot, M. Servillat, N. A. Webb, and R. E. Rutledge, *Astrophys. J.* **772**, 7 (2013).
47. J. M. Lattimer and A. W. Steiner, [arxiv.org:1305.3242](https://arxiv.org/abs/1305.3242) (2013).
48. J. M. Dickey and F. J. Lockman, *Annu. Rev. Astron. Astrophys.* **28**, 215 (1990).
49. D. Haggard, A. M. Cool, J. Anderson, P. D. Edmonds, P. J. Callanan, *et al.*, *Astrophys. J.* **613**, 512 (2004).
50. A. W. Steiner, J. M. Lattimer, and E. F. Brown, *Astrophys. J. Lett.* **765**, 5 (2013).
51. V. Suleimanov, J. Poutanen, M. Revnivtsev, and K. Werner, *Ap. J* **742**, 122 (2011).